Electronic Research Archive

http://www.aimspress.com/journal/era

ERA, 34(1): 251–290.
DOI: 10.3934/era.2026013
Received: 03 November 2025
Revised: 08 December 2025
Accepted: 23 December 2025
Published: 07 January 2026

Research article

Algebraic–spectral thresholds and discrete–continuous stability transfer in Leslie–Gower systems

Louis Shuo Wang[1,†] **and Jiguang Yu**[2,3,†,*]

[1] Department of Mathematics, University of Tennessee, Knoxville, TN 37996, USA
[2] College of Engineering, Boston University, Boston, MA 02215, USA
[3] Department of Mathematics, University College London, London, WC1E 6BT, UK

† The authors contributed equally to this work.

* **Correspondence:** Email: jyu678@bu.edu.

Abstract: We studied an intraguild–predation system where an intermediate consumer and a top consumer exploit a shared basal resource. A compact nondimensionalization yielded five interpretable parameters—relative predator growth α, crowding β, enrichment γ, and depletion couplings δ, ε. We presented closed-form thresholds that organize the dynamics: the coexistence equilibrium exists exactly when a quadratic in the resource steady state has a root in $(0, \beta)$; as γ varies, a two-equilibria window appears and terminates at an explicit saddle–node value γ_1^+, with transversality confirmed and transcritical/pitchfork alternatives excluded. A Hopf onset criterion was given via the characteristic polynomial coefficients along the interior branch. For the forward-Euler discretization we established positivity, an absorbing set under an explicit stepsize bound, and stability tests that reduce to $|1 + \Delta\tau\lambda| = 1$. Extensions to diffusion and stochastic forcing suggest the incorporation of more realistic spatial and stochastic factors. The thresholds were directly calibratable, enabling reproducible, mechanistic predictions for applied systems.

Keywords: algebraic elimination; saddle–node and Hopf bifurcation; Euler discretization; intraguild predation

1. Introduction

The study of ecological systems has been profoundly shaped by the pioneering works of Lotka [1, 2] and Volterra [3]. They introduced mathematical frameworks to describe the interactions between species in ecosystems. Their models laid the foundation for theoretical ecology, a field concerned with understanding how populations of different species interact through mechanisms such as predation,

competition, and cooperation [4, 5]. In particular, three primary types of population interactions are recognized: (i) prey-predator interactions, where one species depends on the other for survival, (ii) competition, where populations vie for limited resources, and (iii) cooperation, where species benefit from mutual existence [6].

Among the various ecological models, those exploring intraguild predation (IGP) have attracted significant attention due to their complexity and relevance to real-world ecosystems. In IGP systems, three species are involved: a basal resource, an intermediate IG-prey that consumes the basal resource, and a top predator that preys on both the resource and the IG-prey. In this framework, the top predator competes with the IG-prey for the same resource while also preying on it, leading to a combination of predation and competition within the system. IGP is a common ecological phenomenon, with significant implications for community structure and species coexistence [7–9]. It is reported to reach frequencies between 58.4% and 86.7% in ecological systems [10]. The classic theory by Holt and Polis [11] predicts that coexistence of species in IGP systems is possible only if the IG-prey is a sufficiently strong competitor for the basal resource.

Predator–prey models differ in how they represent the predator's carrying capacity: the classical Lotka–Volterra model assumes it is constant, whereas Leslie-type models (e.g., Leslie–Gower) treat it as proportional to prey density [12]. Considerable mathematical attention has also been devoted to intraguild predation models [13–15]. For instance, Holling type-I [16], type-II [17, 18], and type-III [19] functional responses are common approaches for different intake rates of predators. Sen et al. [20] analyzed a system with a Holling type-II functional response and demonstrated the emergence of chaotic dynamics through period-doubling bifurcations. More recently, Shang and Qiao [21] incorporated both the fear effect and nonlinear top-predator harvesting, revealing periodic windows and chaotic attractors. Chakravarty et al. [22] inspected the optimal harvesting policy by Pontryagin's maximum principle. Reaction-diffusion systems [23–25] or chemotaxis systems [26, 27] are utilized to incorporate anti-predator strategy. Recent literature has significantly expanded the theoretical framework of predator-prey and Leslie-Gower-type models by incorporating increasingly complex biological mechanisms. For instance, the effects of nonlocal competition have been rigorously analyzed in conjunction with Beddington-DeAngelis functional responses and fear effects, revealing rich bifurcation structures and spatially inhomogeneous solutions [28–30]. Furthermore, the interplay between spatial dynamics and double Allee effects has been shown to generate diverse Turing patterns [31]. Despite these advances in continuous and spatial modeling, there remains a need for rigorous discrete-time frameworks that can bridge deterministic bifurcation theory with stochastic population variability. Safuan et al. [32] proposed a model where the carrying capacities of both the IG-prey and IG-predator depend on a shared resource. They showed that changes in the enrichment parameter can trigger transcritical and Hopf bifurcations, leading to coexistence, prey extinction, or oscillatory dynamics. Yao and Yuan [33] further identified a saddle-node bifurcation and excluded transcritical or pitchfork types, elucidating the catastrophic collapse of the IG-prey population.

While continuous models effectively describe transient dynamics, discrete-time dynamical systems provide a natural and computationally efficient framework. They are well suited for modeling biological, ecological, and regulatory processes that evolve in periodic or generational steps. Discrete formulations not only retain the essential biological structure but also reveal richer dynamical behaviors. These include period-doubling, Neimark–Sacker bifurcation, and chaotic regimes—features that cannot be inferred directly from their continuous analogues [34, 35]. To

further account for population-level randomness, we introduce demographic noise into the discrete framework to represent finite-population fluctuations absent in the deterministic description. This stochastic extension, formulated through diffusion approximation of Poisson events, enables the quantification of demographic noise and is extensible to incorporate biological realism. Building upon the continuous-time bifurcation analysis of Yao and Yuan [33], our study develops a discrete-time and stochastic extension. This extension includes rigorous stability characterization, algebraic–spectral threshold (AST) detection, and comprehensive numerical validation. Our innovations include:

1). Discrete-map formulation. We derive and analyze the forward-Euler discrete map associated with the continuous ODE system. The resulting difference equations preserve the biological constraints of nonnegativity and boundedness, thereby enabling a rigorous study of stability and bifurcation phenomena in the discrete setting.

2). AST algorithm. We develop an explicit computational algorithm that identifies equilibrium transitions and bifurcation thresholds via algebraic coefficients and spectral radii of the Jacobian. Unlike standard numerical continuation methods (e.g., path-following solvers like AUTO or MatCont) that rely on iterative convergence and local derivatives, the AST algorithm exploits closed-form algebraic conditions, specifically discriminants and trace/determinant criteria, to derive exact dynamical boundaries. This yields two distinct advantages: it allows for the global characterization of the parameter space without initialization sensitivity and significantly reduces computational cost by bypassing the need for extensive transient simulations to determine stability. Consequently, the approach provides a simple but robust diagnostic tool to classify dynamical regimes (single equilibrium, bistability, double equilibrium, or no equilibrium) and to precisely detect saddle–node, flip, and Neimark–Sacker bifurcations.

3). Dissipativity and numerical validation. We establish the dissipativity of the discrete map and verify the asymptotic behavior of trajectories across representative parameter regimes. Extensive numerical simulations confirm the analytical predictions and illustrate the correspondence between algebraic thresholds and qualitative dynamical transitions.

4). Demographic noise extension. We incorporate demographic noise into the discrete framework to capture finite-population fluctuations. The resulting stochastic model, formulated as multiplicative Itô–stochastic differential equations (SDEs) with corresponding Fokker–Planck dynamics, links deterministic bifurcation analysis with stochastic population variability and extinction risk.

Methodologically, the derivation of explicit algebraic thresholds bridges the gap between forward bifurcation analysis and the inverse problem of parameter identification. In broader mathematical contexts, inferring system properties from incomplete or noisy observational data remains a central challenge. Recent advances have addressed this through Bayesian methods for recovering scattering obstacles in inhomogeneous media [36], and stable neural network architectures designed to handle contaminated data [37]. Parallel to these data-driven approaches, analytical breakthroughs in inverse spectral problems [38] have demonstrated how incomplete spectral data can rigorously reconstruct underlying operators. Analogous to how asymptotic and effective medium theories provide rigorous frameworks for resolving electromagnetic inverse scattering and field blow-up [39, 40], our AST framework utilizes the algebraic structure of the Jacobian to "invert" observed ecological tipping

points. By providing exact closed-form constraints, the AST offers a deterministic prior that can enhance the interpretability and robustness of multi-scale inversion algorithms applied to ecological time series.

To this end, we formalize the IGP model in Section 2, and discuss the local bifurcation results in Section 3. The discrete Euler map and its properties is presented in Section 4, and the stochastic extension is in Section 5. We present numerical simulation results in Section 6. We conclude the work in Section 7.

2. Model and nondimensionalization

2.1. Dimensional model and biological assumptions

We consider a three-compartment intraguild system comprising a basal prey $n(t_d)$, an intraguild predator $p(t_d)$, and a limiting resource $r(t_d)$ that modulates crowding in both consumer populations. The governing equations are

$$\begin{aligned} \frac{dn}{dt_d} &= r_1 n\left(1-\frac{n}{r}\right)-\eta np,\\ \frac{dp}{dt_d} &= r_2 p\left(1-\frac{\beta_d p}{r}\right)+\eta np,\\ \frac{dr}{dt_d} &= \rho r(\Gamma-\delta_d n-\epsilon_d p), \end{aligned} \tag{2.1}$$

with initial data $(n(0), p(0), r(0)) \in \mathbb{R}^3_{\geq 0}$. All parameters are strictly positive. The terms are interpreted as follows:

(i) The prey n displays logistic growth with intrinsic rate r_1 and resource-limited carrying capacity proportional to r, hence the factor $1 - n/r$.

(ii) The predator p has intrinsic (baseline) reproduction r_2 and self-crowding proportional to p/r, with coefficient β_d. In addition, predator biomass increases through intraguild predation at the bilinear rate ηnp, which is mirrored by a loss term in the prey.

(iii) The resource r turns over at rate ρ, is supplied at an enrichment level Γ, and is linearly depleted by consumers with per-capita intensities δ_d (prey) and ϵ_d (predator).

The dimensional parameters and their interpretations are summarized in Table 1.

Table 1. Dimensional parameters used in Eq (2.1). All parameters are positive.

Symbol	Meaning (dimensional)
r_1	prey intrinsic growth rate
r_2	predator intrinsic growth rate
η	intraguild predation/transfer coefficient
β_d	predator crowding coefficient relative to r
ρ	resource turnover rate
Γ	dimensional enrichment/supply rate
δ_d, ϵ_d	resource depletion per prey/predator individual

A prototypical real-world realization of this model is the aquatic food web of Lake Kinneret (Israel) [41]. In this system, the limiting resource r corresponds to herbivorous zooplankton, which serves as the basal food source. The population n represents predatory invertebrates (specifically cyclopoid copepods), which act as the intermediate consumer feeding on the zooplankton. The intraguild predator p corresponds to planktivorous fish (e.g., *Mirogrex terraesanctae*), which are generalist feeders consuming both the zooplankton and the copepods. The Leslie-Gower formulation is particularly appropriate for this ecosystem because the fish population relies heavily on the abundant basal zooplankton. Consequently, following the modeling principles of [42], we define the predator's carrying capacity as a function of the limiting basal resource r.

We briefly discuss the Leslie-Gower model, which offers several advantages over Holling or generalized functional responses. First, it captures the ecological context for generalist predators. In ecosystems such as the Lake Kinneret aquatic food web, the top predator (planktivorous fish) is a generalist that feeds on both the intermediate consumer (copepods) and the basal resource (zooplankton); the Leslie-Gower formulation is particularly appropriate for such structures. Second, it enables the modeling of carrying capacity via shared resources. Unlike standard Lotka-Volterra or Holling models, which often assume constant carrying capacity, the Leslie-Gower framework allows the predator's carrying capacity to be defined as a function of the limiting basal resource r. Third, it models the dependency on abundant basal resources. In Lake Kinneret, the fish population relies heavily on the abundant basal zooplankton. Therefore, a realistic model must account for the carrying capacity being proportional to this resource density (represented by the term $1 - \frac{\beta_d p}{r}$).

We justify the assumption that both consumers (n and p) experience crowding relative to r based on the specific biological characteristics of the generalist IGP system we model:

(i) For the intermediate consumer n, this species (e.g., copepods) is a strict consumer of the basal resource (r, zooplankton). Therefore, it is biologically standard to model its carrying capacity as directly proportional to the abundance of its limiting resources, leading to the logistic term $1 - n/r$.

(ii) For the top predator p, the species in our specific system (e.g., plantkivorous fish) is a generalist that feeds on both the intermediate consumer n and the basal resource r. Since the fish relies heavily on the abundant basal zooplankton, and this basal resource constitutes a significant portion of the energy budget for both species, r sets the environmental carrying capacity for both. The Leslie-Gower formulation $1 - \beta_d p/r$ captures this dual dependency, reflecting that the predator's upper limit is constrained primarily by the availability of the shared basal resource rather than solely by the density of the intermediate prey.

2.2. Scaling and nondimensional equations

We nondimensionalize time and state variables so that the predation transfer becomes a unit-coefficient and the crowding terms appear as N/R and P/R.

For the time scale, let

$$\tau := r_1 t_d.$$

For population and resource scales, set a common biomass scale:

$$B := \frac{r_1}{\eta}, \quad R_* := \frac{r_1}{\eta},$$

and define nondimensional variables

$$N(\tau) := \frac{n(t_d)}{B}, \quad P(\tau) := \frac{p(t_d)}{B}, \quad R(\tau) := \frac{r(t_d)}{R_*}.$$

With these choices, substituting $n = BN$, $p = BP$, $r = R_*R$ into (2.1) and using $d/d\tau = (1/r_1)d/dt_d$ yield

$$\begin{aligned} \frac{dN}{d\tau} &= N\left(1 - \frac{N}{R}\right) - NP, \\ \frac{dP}{d\tau} &= \alpha P\left(1 - \frac{\beta P}{R}\right) + NP, \\ \frac{dR}{d\tau} &= R(\gamma - \delta N - \epsilon P), \end{aligned} \tag{2.2}$$

where the dimensionless parameters are

$$\alpha := \frac{r_2}{r_1}, \qquad \beta := \beta_{\mathrm{d}}, \qquad \gamma := \frac{\rho}{r_1}\Gamma, \qquad \delta := \frac{\rho}{\eta}\delta_{\mathrm{d}}, \qquad \epsilon := \frac{\rho}{\eta}\epsilon_{\mathrm{d}}. \tag{2.3}$$

All five parameters $\alpha, \beta, \gamma, \delta, \epsilon$ are positive and will be treated as free bifurcation and regime parameters in what follows. The chosen scaling enforces a unit predation transfer coefficient and uses the resource itself as the crowding currency in both consumers.

For compactness, we will therefore relabel τ as t and write the nondimensional system as

$$\begin{aligned} \dot{N} &= N\left(1 - \frac{N}{R}\right) - NP, \\ \dot{P} &= \alpha P\left(1 - \frac{\beta P}{R}\right) + NP, \qquad (N, P, R)(0) \in \mathbb{R}^3_{\geq 0}. \\ \dot{R} &= R(\gamma - \delta N - \epsilon P), \end{aligned} \tag{2.4}$$

We also introduce the vector notation

$$X := (N, P, R)^\top, \quad \dot{X} = F(X; \theta), \quad \theta := (\alpha, \beta, \gamma, \delta, \epsilon) \in \mathbb{R}^5_{>0}.$$

Remark 2.1 (On the choice of scales)**.** *The scaling $B = R_* = r_1/\eta$ is not unique but is particularly convenient. (i) It normalizes the predation/transfer term to NP. (ii) It preserves the transparent "resource-limited" logistic forms $1 - N/R$ and $1 - \beta P/R$. (iii) It expresses the resource dynamics in multiplicative form $R(\cdot)$, which guarantees positivity of R for positive initial data. Alternative choices are possible (e.g., absorbing β into the predator scale), but* (2.4) *is the most parsimonious for analysis.*

Remark 2.2 (Domain and invariance)**.** *Because the right-hand side of* (2.4) *is locally Lipschitz on $\{R > 0\}$, a unique solution exists and remains in the nonnegative orthant provided $R(0) > 0$. The plane $R = 0$ is invariant and attracts no trajectory with $R(0) > 0$ due to the multiplicative factor R in $\dot{R}$. Moreover, the coordinate planes $N = 0$ and $P = 0$ are also invariant since $\dot{N}|_{N=0} = 0$ and $\dot{P}|_{P=0} = 0$. Therefore, the unique solution $(N(t), P(t), R(t))$ starting from $(N(0), P(0), R(0)) \in \mathbb{R}^3_{>0}$ will*

remain in $\mathbb{R}^3_{>0}$. *The forward invariance of* $\mathbb{R}^3_{>0}$ *can also be deduced from the following formulas for* $(N(t), P(t), R(t))$*: for all* $t \geq 0$ *in the existence interval,*

$$N(t) = N(0)\exp\left(\int_0^t \left(1 - \frac{N(\tau)}{R(\tau)} - P(\tau)\right)d\tau\right),$$

$$P(t) = P(0)\exp\left(\int_0^t \alpha\left(1 - \frac{\beta P(\tau)}{R(\tau)} + N(\tau)\right)d\tau\right),$$

$$R(t) = R(0)\exp\left(\int_0^t \left(\gamma - \delta N(\tau) - \epsilon P(\tau)\right)d\tau\right).$$

In the remainder of the paper, we denote equilibria of (2.4) by $\mathcal{E}_1$, $\mathcal{E}_2$, $\mathcal{E}_3$ (as applicable). They are ordered by biological interpretation, distinguishing boundary equilibria from interior coexistence states. We also use this nondimensionalization consistently across the continuous-time and spatial/stochastic extensions. Table 2 lists dimensionless parameters.

Table 2. Dimensionless parameters appearing in (2.4). All are strictly positive.

Symbol	Role in (2.4)	Definition in terms of (2.1)
α	predator intrinsic rate relative to the prey's	r_2/r_1
β	predator self-crowding vs. resource	β_d
γ	enrichment/resource supply	$(\rho/r_1)\Gamma$
δ	resource depletion by prey	$(\rho/\eta)\delta_d$
ϵ	resource depletion by predator	$(\rho/\eta)\epsilon_d$

3. Equilibria and local bifurcations

Recall the nondimensional system (2.4) derived in Section 2, with parameters $\theta = (\alpha, \beta, \gamma, \delta, \epsilon) \in \mathbb{R}^5_{>0}$. We denote equilibria of (2.4) by $\mathcal{E} = (N^*, P^*, R^*)$.

3.1. Boundary and interior equilibria

Setting $f_1 = f_2 = f_3 = 0$ with one or more coordinates equal to zero yields two biologically relevant boundary equilibria.

(i) **IG-prey only**:

$$\mathcal{E}_1 = \left(\frac{\gamma}{\delta},\, 0,\, \frac{\gamma}{\delta}\right).$$

At $\mathcal{E}_1$, the IG-predator P is absent. Linearization gives three eigenvalues,

$$\operatorname{spec}(J(\mathcal{E}_1)) = \left\{\alpha + \frac{\gamma}{\delta}, -\frac{1}{2} \pm \frac{1}{2}\sqrt{1 - 4\gamma}\right\},$$

so $\mathcal{E}_1$ is unstable, since the first eigenvalue $\alpha + \gamma/\delta > 0$.

(ii) **IG-predator only**:

$$\mathcal{E}_2 = \left(0, \frac{\gamma}{\epsilon}, \frac{\beta\gamma}{\epsilon}\right).$$

Here, the IG-prey N is extinct, and the IG-predator P coexists with the resource. $\mathcal{E}_2$ has the characteristic equation

$$\lambda^3 + \Big(\alpha - 1 + \frac{\gamma}{\epsilon}\Big)\lambda^2 + \Big(\frac{\alpha(\gamma - \epsilon - \gamma\epsilon)}{\epsilon}\Big)\lambda + \frac{\alpha\gamma(\gamma - \epsilon)}{\epsilon} = 0,$$

and the eigenvalues for $\mathcal{E}_2$ are

$$\text{spec}(J(\mathcal{E}_2)) = \Big\{1 - \frac{\gamma}{\epsilon}, -\frac{\alpha}{2} \pm \frac{1}{2}\sqrt{\alpha(\alpha - 4\gamma)}\Big\}.$$

The first eigenvalue crosses 0 at $\gamma = \epsilon$, the predator-only threshold. From the spectral information of $\mathcal{E}_2$, $\mathcal{E}_2$ is stable if $\gamma > \epsilon$ and unstable if $\gamma < \epsilon$. The condition $\gamma > \epsilon$ ensures that the predator-only equilibrium is stable by maintaining a predator density $P^* = \gamma/\epsilon > 1$. Since the dimensionless prey intrinsic growth rate is 1, this inequality implies that the resource enrichment γ is sufficiently high to sustain a predator population whose consumption pressure overwhelms the prey's reproductive potential, leading to the competitive exclusion of the mesopredator.

Next we study interior (coexistence) equilibria $\mathcal{E}_3 = (N^*, P^*, R^*)$ with $N^*, P^*, R^* > 0$. Solving $f_1 = 0$ and $f_2 = 0$ gives

$$P^* = 1 - \frac{N^*}{R^*}, \qquad \alpha\Big(1 - \frac{\beta P^*}{R^*}\Big) + N^* = 0,$$

from which one finds

$$N^* = \frac{\alpha R^*(\beta - R^*)}{R^{*2} + \alpha\beta}, \qquad P^* = \frac{R^*(\alpha + R^*)}{R^{*2} + \alpha\beta}.$$

Finally, $f_3 = 0$ yields $\gamma - \delta N^* - \epsilon P^* = 0$, which, after substitution of the above expressions of N^* and P^*, reduces to a quadratic equation for R^*:

$$c_1 R^2 + c_2 R + c_3 = 0, \qquad c_1 = \frac{\gamma - \epsilon}{\alpha} + \delta, \quad c_2 = -(\beta\delta + \epsilon), \quad c_3 = \beta\gamma. \tag{3.1}$$

Therefore, we can express the interior equilibrium of (2.4) as

$$\mathcal{E}_3 = \Big(\frac{\alpha R^*(\beta - R^*)}{R^{*2} + \alpha\beta}, \frac{R^*(\alpha + R^*)}{R^{*2} + \alpha\beta}, R^*\Big), \tag{3.2}$$

and each interior equilibrium corresponds exactly to the positive roots of the quadratic (3.1). The positivity of $\mathcal{E}_3$ requires

$$R^* \in (0, \beta).$$

We determine the number of interior equilibria, which depends on the discriminant $\Delta = c_2^2 - 4c_1c_3$ and the sign of c_1. Since $c_3 = \beta\gamma > 0$, the quadratic has either two positive roots, one positive (and one negative) root, or no real positive roots. A detailed analysis shows the following results.

Theorem 3.1. *[33][A positive equilibrium when $\gamma \le \epsilon$] Assume all parameters $\alpha, \beta, \gamma, \delta, \epsilon$ in model* (2.4) *are positive. If (i) $\gamma < \epsilon$ or (ii) $\gamma = \epsilon$ and $\beta\delta > \epsilon$, then* (2.4) *admits a unique interior equilibrium $\mathcal{E}_3 = (N^*, P^*, R^*) \in (0, \infty)^3$. In case (i), this root arises from the quadratic* (3.1) *having one positive and one negative root, and in case (ii), it arises from one positive root with one root zero. No other positive equilibria exist in these cases.*

Theorem 3.1 covers all cases where $\gamma \le \epsilon$ (except the degenerate case $\gamma = \epsilon$ with $\beta\delta = \epsilon$, which yields a triple degeneracy at $\mathcal{E}_2$). Next, when $\gamma > \epsilon$, we can have two interior equilibria. One finds that two positive roots of (3.1) occur precisely when $c_1 > 0$ and $\Delta \ge 0$. The following establishes the condition for two interior equilibria:

Lemma 3.1. *[33][Two interior equilibria for $\gamma > \epsilon$] Fix $\alpha, \beta, \delta, \epsilon > 0$. Consider* (2.4) *and let c_1, c_2, c_3 be given in* (3.1) *so that any interior equilibrium has its third coordinate R^* solving*

$$c_1 R^2 + c_2 R + c_3 = 0.$$

Define the concave quadratic

$$\Delta(\gamma) := c_2^2 - 4c_1c_3 = -\frac{4\beta}{\alpha}\gamma^2 + 4\beta\Big(\frac{\epsilon}{\alpha} - \delta\Big)\gamma + (\beta\delta + \epsilon)^2,$$

and let $\gamma_1^{\pm}$ denote the two real roots of $\Delta(\gamma) = 0$, namely

$$\gamma_1^{\pm} = \frac{\alpha}{2}\left(\frac{\epsilon}{\alpha} - \delta \pm \sqrt{\Big(\frac{\epsilon}{\alpha} - \delta\Big)^2 + \frac{(\beta\delta + \epsilon)^2}{\alpha\beta}}\right), \tag{3.3}$$

so that $\gamma_1^- < 0 < \gamma_1^+$. Set also

$$\gamma_2 = \frac{\epsilon^2 + \beta\delta\epsilon}{2\beta\delta}.$$

Then, for the parameter γ, (2.4) *admits exactly two interior equilibria if and only if*

$$\max\{\epsilon, \gamma_2\} < \gamma < \gamma_1^+.$$

Remark 3.1 (Saddle-node at the upper endpoint)**.** *At $\gamma = \gamma_1^+$ the reduced quadratic in R has a double positive root R^*, and hence the two interior equilibria coalesce into a single interior equilibrium $\mathcal{E}_3^* = (N^*, P^*, R^*)$. It has been shown in Theorem 3.3 that $\mathcal{E}_3^*$ is a saddle-node: the Jacobian at $\mathcal{E}_3^*$ has a simple zero eigenvalue while the remaining eigenvalues have nonzero real parts, and the standard transversality condition holds. Consequently, as γ increases through γ_1^+, the pair of interior equilibria is created/destroyed in a saddle-node bifurcation.*

Theorem 3.2. *[33][Sharp condition for the existence of two interior equilibria] Let $\alpha, \beta, \delta, \epsilon > 0$. For* (2.4)*, define*

$$\gamma_2 = \frac{\epsilon^2 + \beta\delta\epsilon}{2\beta\delta}, \quad \gamma_1^{\pm} = \frac{\alpha}{2}\left(\frac{\epsilon}{\alpha} - \delta \pm \sqrt{\Big(\frac{\epsilon}{\alpha} - \delta\Big)^2 + \frac{(\beta\delta + \epsilon)^2}{\alpha\beta}}\right).$$

Thus $\gamma_1^- < 0 < \gamma_1^+$. By Lemma 3.1, the system has two interior equilibria precisely for

$$\gamma \in \Big(\max\{\epsilon, \gamma_2\}, \gamma_1^+\Big).$$

There exists at least one γ with $\epsilon < \gamma < \gamma_1^+$ such that (2.4) *has two interior equilibria if and only if*

$$\beta\delta > \epsilon.$$

From Theorem 3.2 we see that when $\beta\delta > \epsilon$ and γ lies in (ϵ, γ_1^+), two interior equilibria appear. When $\beta\delta > \epsilon$ and γ exceeds γ_1^+, the two equilibria collide and disappear; this collision at $\gamma = \gamma_1^+$ is exactly a saddle–node bifurcation, as we establish below. For clarity, we restate the parameter-dependent outcomes for the number of interior equilibria:

Corollary 3.1 (Complete count of interior equilibria)**.** *Let $\alpha, \beta, \delta, \epsilon > 0$, and γ_1^+, γ_2 are as above. Then:*

(i) If either $\beta\delta \le \epsilon$ and $\gamma < \epsilon$, or $\beta\delta > \epsilon$ with $\gamma \le \epsilon$, (2.4) *admits exactly one biologically relevant (positive) equilibrium.*

(ii) If $\beta\delta > \epsilon$ and the enrichment parameter lies within the open interval $\epsilon < \gamma < \gamma_1^+$, two distinct interior equilibria coexist.

(iii) At the threshold value $\gamma = \gamma_1^+$, still with $\beta\delta > \epsilon$, these two equilibria merge into a single degenerate (double) equilibrium.

(iv) When γ exceeds γ_1^+ (for $\beta\delta > \epsilon$), or when $\beta\delta \le \epsilon$ together with $\gamma \ge \epsilon$, no positive equilibrium persists.

In summary, depending on the parameter ordering of $(\beta\delta, \epsilon, \gamma)$, the model supports either zero, one, or two interior equilibria, with the collision at $\gamma = \gamma_1^+$ marking the onset of the saddle–node bifurcation.

Ecologically, the emergence of dual interior equilibria corresponds to a regime of bistability created by a separatrix. The unstable interior equilibrium acts as a critical threshold separating the basin of attraction for species coexistence from that of IG-prey exclusion $\mathcal{E}_2$. This implies priority effects, where the system's long-term state is determined by initial population densities rather than environmental carrying capacities alone. If the initial populations (N_0, P_0) are above this separatrix, the system flows to the coexistence state. If they are below it (e.g., the IG-prey density is too low), the system is pulled into the predator-only state.

Furthermore, the saddle-node bifurcation at $\gamma = \gamma_1^+$ identifies a catastrophic tipping point driven by resource enrichment. If the enrichment rate γ exceeds this critical threshold, the coexistence window vanishes abruptly, forcing the IG-prey to extinction. Unlike gradual declines observed in other bifurcation scenarios, this transition is discontinuous and hysteretic; once the species is lost, simply reducing the enrichment parameter γ back below γ_1^+ is insufficient to recover the coexistence state, as the system remains trapped in the predator-only attractor.

Remark 3.2 (Degeneracy at the prey-free point when $\beta\delta = \gamma = \epsilon$)**.** *When $\beta\delta = \epsilon$ and $\gamma = \epsilon$, the reduced equilibrium equations collapse to*

$$c_1(R - \beta)^2 = 0.$$

Thus, the prey-free equilibrium $\mathcal{E}_2 = (0, 1, \beta)$ becomes degenerate, and the associated R-quadratic has a double root at $R = \beta$. This is the natural boundary between the regimes.

Having classified the number of equilibria, we next analyze their local stability and bifurcation structure. We focus first on the saddle–node bifurcation that occurs at $\gamma = \gamma_1^+$. Let $\mathcal{E}_3 = (N^*, P^*, R^*)$

denote a positive equilibrium of (2.4) when it exists. The Jacobian of (2.4) at $\mathcal{E}_3$ is

$$J = \begin{pmatrix} 1 - 2N^*/R^* - P^* & -N^* & \frac{N^{*2}}{R^{*2}} \\ P^* & \alpha - 2\alpha\beta P^*/R^* + N^* & \frac{\alpha\beta P^{*2}}{R^{*2}} \\ -\delta R^* & -\epsilon R^* & \gamma - \delta N^* - \epsilon P^* \end{pmatrix}.$$

Using the steady state equations $f_1(\mathcal{E}_3) = f_2(\mathcal{E}_3) = f_3(\mathcal{E}_3) = 0$, the characteristic polynomial is simplified as

$$\lambda^3 + a_1\lambda^2 + a_2\lambda + a_3 = 0,$$

with

$$a_1 = \frac{N^* + \alpha\beta P^*}{R^*}, \quad a_2 = N^*P^* + \frac{\delta N^{*2} + \alpha\beta\epsilon P^{*2}}{R^*} + \frac{\alpha\beta N^*P^*}{R^{*2}},$$
$$a_3 = \frac{N^*P^*}{R^{*2}}\Big(\alpha\beta\delta N^* + \epsilon N^*R^* + \alpha\beta\epsilon P^* - \alpha\beta\delta P^*R^*\Big).$$

One can show that $a_1 > 0$ and $a_2 > 0$ whenever an equilibrium exists, so Routh-Hurwitz tells us:

$$\text{(ODE stability)} \implies a_1 > 0, a_2 > 0, a_3 > 0, \text{ and } a_1a_2 > a_3.$$

A saddle–node bifurcation occurs when the Jacobian has a simple zero eigenvalue. Indeed, one finds that at $\gamma = \gamma_1^+$, $\Delta = 0$ and the quadratic (3.1) has a double root $R^* = (\beta\delta + \epsilon)/[2(\frac{\gamma_1^+ - \epsilon}{\alpha} + \delta)]$, and one checks that the corresponding $\mathcal{E}_3$ makes $a_3 = 0$. To make this explicit, we rewrite a_3 in a factored form. Starting from its definition,

$$a_3 = \frac{N^*P^*}{R^{*2}}\Big(\alpha\beta\delta N^* + \epsilon N^*R^* + \alpha\beta\epsilon P^* - \alpha\beta\delta P^*R^*\Big),$$

and using the equilibrium relations

$$N^* = \frac{\alpha R^*(\beta - R^*)}{R^{*2} + \alpha\beta}, \qquad P^* = \frac{R^*(\alpha + R^*)}{R^{*2} + \alpha\beta},$$

we can simplify the parentheses as

$$\alpha\beta\delta N^* + \epsilon N^*R^* + \alpha\beta\epsilon P^* - \alpha\beta\delta P^*R^* = \frac{\alpha N^*P^*}{R^*(\alpha\beta + R^{*2})}\Big[-(\epsilon + \beta\delta)R^{*2} + 2\beta(\epsilon - \alpha\delta)R^* + \alpha\beta(\beta\delta + \epsilon)\Big].$$

The prefactor $\dfrac{\alpha N^*P^*}{R^*(\alpha\beta + R^{*2})}$ is strictly positive for an interior equilibrium $R^* \in (0, \beta)$, so the sign of a_3 is determined by the last bracket. Therefore, $a_3 = 0$ when

$$R^* = \frac{\beta\epsilon - \alpha\beta\delta + \alpha\beta\sqrt{(\frac{\epsilon}{\alpha} - \delta)^2 + \frac{1}{\alpha\beta}(\beta\delta + \epsilon)^2}}{\beta\delta + \epsilon}$$
$$= \frac{\alpha\beta(\beta\delta + \epsilon)}{\alpha\beta\sqrt{(\frac{\epsilon}{\alpha} - \delta)^2 + \frac{1}{\alpha\beta}(\beta\delta + \epsilon)^2} + \alpha\beta\delta - \beta\epsilon} = \frac{\beta\delta + \epsilon}{2(\frac{\gamma_1^+ - \epsilon}{\alpha} + \delta)}.$$

$a_3 = 0$ ensures that one eigenvalue crosses zero at γ_1^+, while the other two eigenvalues remain nonzero. By Sotomayor's theorem (e.g., [43]), this zero-eigenvalue crossing is generically a saddle–node bifurcation, provided a certain nondegeneracy condition $\Theta \neq 0$ holds. Originating from the second-order Taylor expansion of the vector field F, Θ quantifies the nonlinear curvature of the dynamics along the critical direction. A calculation (detailed in [33]) shows that the required nondegeneracy factor $\Theta \propto W^T \cdot \Big[D^2F(\mathcal{E}_3, \gamma_1^+)[V, V]\Big]$ is nonzero, where W, V are the left and right nullvectors of the Jacobian matrix at $\mathcal{E}_3$, $J(\mathcal{E}_3, \gamma_1^+)$, respectively. Physically, this non-zero curvature ensures that the destruction of the coexistence state is sharp rather than flat; it dictates that the resilience of the system (measured by the rate of return, i.e., absolute magnitude of the real part of the dominant eigenvalue $|\Re(\lambda)|$) vanishes as a square-root function $\sqrt{|\gamma - \gamma_1^+|}$ as the tipping point is approached. We therefore conclude:

Theorem 3.3. *[33][Saddle-node at the interior equilibrium; exclusion of transcritical/pitchfork] Let γ be the bifurcation parameter and let γ_1^+ be the critical value defined in* (3.3). *Suppose $\mathcal{E}_3 = (N^*, P^*, R^*) \in (0, \infty)^3$ is the interior equilibrium of* (2.4) *corresponding to $\gamma = \gamma_1^+$. Let U and W be the right and left eigenvectors of the zero eigenvalues of $J(\mathcal{E}_3, \gamma_1^+)$:*

$$J(\mathcal{E}_3, \gamma_1^+)U = 0, \quad W^\top J(\mathcal{E}_3, \gamma_1^+) = 0.$$

Then:

(i) (Exclusion of transcritical/pitchfork). The transversality condition holds:

$$W^\top F_\gamma(\mathcal{E}_3, \gamma_1^+) = w_3 R^* \neq 0, \ \text{for } W = (w_1, w_2, w_3).$$

Therefore, no transcritical or pitchfork bifurcation occurs at $(\mathcal{E}_3, \gamma_1^+)$;

(ii) (Saddle-node). If the coefficient $\Theta \neq 0$, where

$$\Theta = \frac{-2\epsilon P^*}{N^*}\left[\Big(\frac{N^*(\alpha\beta + R^{*2})}{\alpha\beta(N^* - P^*R^*)} - 1\Big)^2 - \frac{R^*}{\beta(N^* - P^*R^*)}\right] + \frac{2N^*(P^*(\alpha\beta + R^*) - \alpha)^2}{\alpha\beta R^*(N^* - P^*R^*)^2}$$
$$- \alpha R^* - \frac{2R^*(\alpha\beta + R^{*2})}{\alpha\beta}\left(\delta + \frac{\epsilon}{\beta(N^* - P^*R^*)}\right),$$

then the nondegeneracy condition

$$W^\top\Big[D^2F(\mathcal{E}_3, \gamma_1^+)(U, U)\Big] \neq 0$$

is satisfied. As a consequence, (2.4) *undergoes a (generic) saddle-node bifurcation at $(\mathcal{E}_3, \gamma_1^+)$.*

Let γ_1^+ be the value defined above. At $\gamma = \gamma_1^+$ (2.4) *undergoes a saddle–node bifurcation at the interior equilibrium $\mathcal{E}_3$. That is, as γ increases through γ_1^+, two interior equilibria collide and disappear (for $\beta\delta > \epsilon$). There is no transcritical or pitchfork bifurcation at $\mathcal{E}_3$ in this process.*

3.2. Hopf criterion and whether it can occur

Let $\chi(\lambda) = \lambda^3 + a_1\lambda^2 + a_2\lambda + a_3$ at an interior equilibrium. The cubic Routh-Hurwitz conditions for linear asymptotic stability are

$$a_1 > 0, \quad a_2 > 0, \quad a_3 > 0, \quad a_1a_2 > a_3.$$

A generic Hopf occurs when a conjugate pair of complex eigenvalues crosses the imaginary axis transversely, while the remaining real eigenvalue remains negative. We next detail the onset of the Hopf bifurcation with respect to the Routh-Hurwitz conditions.

Lemma 3.2. *Let $\mathcal{E}_3 = (N^*, P^*, R^*) \in (0,\infty)^3$ be an interior equilibrium of* (2.4)*. Let the characteristic polynomial of the Jacobian at $\mathcal{E}_3$ be*

$$\chi(\lambda) = \lambda^3 + a_1\lambda^2 + a_2\lambda + a_3,$$

with coefficients

$$a_1 = \frac{N^* + \alpha\beta P^*}{R^*}, \qquad a_2 = N^*P^* + \frac{\delta N^{*2} + \alpha\beta\epsilon P^{*2}}{R^*} + \frac{\alpha\beta N^*P^*}{R^{*2}},$$

$$a_3 = \frac{N^*P^*}{R^{*2}}(\alpha\beta\delta N^* + \epsilon N^*R^* + \alpha\beta\epsilon P^* - \alpha\beta\delta P^*R^*).$$

Then:

(i) $a_1 > 0$ *and* $a_2 > 0$ *whenever an interior equilibrium exists;*

(ii) a (generic) Hopf bifurcation occurs precisely when

$$a_1 > 0, \quad a_2 > 0, \quad a_3 > 0, \quad a_1a_2 = a_3, \quad \partial_\gamma(a_1a_2 - a_3) \neq 0. \tag{3.4}$$

Proof. The first four relations in (3.4) can be deduced by assuming a pair of imaginary roots $i\omega$ with a negative root $\omega' < 0$ and then calculating the characteristic polynomial

$$(\lambda - i\omega)(\lambda + i\omega)(\lambda - \omega') = \lambda^3 - \omega'\lambda^2 + \omega^2\lambda - \omega^2\omega'.$$

We now show that the final inequality $\partial_\gamma(a_1a_2 - a_3) \neq 0$ exactly expresses the transversality condition. Let

$$p(\lambda, \gamma) = \lambda^3 + a_1(\gamma)\lambda^2 + a_2(\gamma)\lambda + a_3(\gamma)$$

be the characteristic polynomial and assume a Hopf point γ_0 where a conjugate pair $\lambda(\gamma_0) = \pm i\omega_0$ ($\omega_0 > 0$) occurs. From $p(i\omega_0, \gamma_0) = 0$ we get the family relations

$$\omega_0^2 = a_2(\gamma_0), \quad a_3(\gamma_0) = a_1(\gamma_0)a_2(\gamma_0).$$

Differentiate the eigenvalue equation $p(\lambda(\gamma), \gamma) = 0$ with respect to γ. By the chain rule,

$$p_\lambda(\lambda, \gamma)\frac{d\lambda}{d\gamma} + p_\gamma(\lambda, \gamma) = 0 \implies \frac{d\lambda}{d\gamma} = -\frac{p_\gamma}{p_\lambda},$$

evaluated at $\lambda = i\omega_0$, $\gamma = \gamma_0$. We will compute the real part of $d\lambda/d\gamma$, which is the rate at which the real part of the eigenvalue moves through zero. Compute p_λ and p_γ at $\lambda = i\omega$ and use $\omega^2 = a_2$:

$$p_\lambda(i\omega) = 3(i\omega)^2 + 2a_1(i\omega) + a_2 = -2\omega^2 + 2ia_1\omega = 2i\omega(a_1 + i\omega),$$

and

$$\begin{aligned} p_\gamma(i\omega) &= a_1'(i\omega)^2 + a_2'(i\omega) + a_3' \\ &= -a_1'\omega^2 + ia_2'\omega + a_3' = ia_2'\omega + (a_3' - a_1'a_2). \end{aligned}$$

Introduce the shorthand

$$\Delta(\gamma) \equiv a_1a_2 - a_3,$$

so $\Delta'(\gamma) = a_1'a_2 + a_1a_2' - a_3'$. Rearranging gives $a_3' - a_1'a_2 = a_1a_2' - \Delta'$. Hence

$$p_\gamma(i\omega) = a_2'(a_1 + i\omega) - \Delta'.$$

Now

$$\left.\frac{d\lambda}{d\gamma}\right|_{\lambda=i\omega} = -\frac{p_\gamma}{p_\lambda} = -\frac{a_2'(a_1 + i\omega) - \Delta'}{2i\omega(a_1 + i\omega)} = -\frac{a_2'}{2i\omega} + \frac{\Delta'}{2i\omega(a_1 + i\omega)}.$$

The first term is purely imaginary, so it does not affect the real part. Taking real parts and using $a_1 + i\omega$ and its conjugate,

$$\Re\Big(\frac{d\lambda}{d\gamma}\Big) = \Re\Big(\frac{\Delta'}{2i\omega(a_1 + i\omega)}\Big) = -\frac{2\omega^2}{|2i\omega(a_1 + i\omega)|^2}\Delta' = -\frac{2\omega^2}{|p_\lambda(i\omega)|^2}\Delta'.$$

Because $\omega^2 > 0$ and $|p_\lambda(i\omega)| > 0$, we conclude

$$\Re(d\lambda/d\gamma) \neq 0 \quad \Longleftrightarrow \quad \Delta'(\gamma) \neq 0,$$

i.e., $\partial_\gamma(a_1a_2 - a_3) \neq 0$ if and only if the real part of the critical eigenvalue changes with γ.

Remark 3.3. *The Hopf condition $a_3 = a_1a_2 > 0$ cannot coincide with the saddle–node value $\gamma = \gamma_1^+$. At γ_1^+ the quadratic defining R^* has a double root, and the corresponding equilibrium satisfies $a_3 = 0$. Since Hopf requires $a_3 > 0$, the two bifurcations are mutually exclusive.*

4. Discrete-time Euler map

Having the local stability and bifurcation structure of (2.4), we translate the results to the discrete Euler map with step size $\Delta\tau > 0$:

$$\begin{aligned} N_{n+1} &= N_n + \Delta\tau(N_n(1 - \tfrac{N_n}{R_n}) - N_nP_n), \\ P_{n+1} &= P_n + \Delta\tau(\alpha P_n(1 - \tfrac{\beta P_n}{R_n}) + N_nP_n), \\ R_{n+1} &= R_n + \Delta\tau R_n(\gamma - \delta N_n - \epsilon P_n). \end{aligned} \tag{4.1}$$

We denote the one-step map by $\Phi_{\Delta\tau} : (N_n, P_n, R_n) \mapsto (N_{n+1}, P_{n+1}, R_{n+1})$.

4.1. Dissipativity and stability

Let $\mathcal{K}(M,m) := \{0 \le N \le M : 0 \le P \le M, m \le R \le M\}$ with $M > m > 0$. We show solutions remain positive on the absorbing set $\mathcal{K}(M,m)$ when $\Delta\tau$ is sufficiently small.

Lemma 4.1 (Conditional positivity on $\mathcal{K}(M,m)$)**.** *Fix $M > m > 0$. If $(N_n, P_n, R_n) \in \mathcal{K}(M,m)$ and*

$$\Delta\tau \le \Delta\tau_{\text{pos}} := \min\left\{\frac{1}{M+\frac{M}{m}},\ \frac{1}{\alpha\beta\frac{M}{m}},\ \frac{1}{\delta M+\epsilon M}\right\}, \tag{4.2}$$

then $(N_{n+1}, P_{n+1}, R_{n+1}) \in \mathbb{R}^3_{\ge 0}$. Moreover, if $R_n \ge m$, then $R_{n+1} \ge m(1-\Delta\tau(\delta M+\epsilon M))$.

Proof. Writing (4.1) in the factorized form

$$\begin{aligned}
N_{n+1} &= N_n\Big(1+\Delta\tau((1-\tfrac{N_n}{R_n})-P_n)\Big),\\
P_{n+1} &= P_n\Big(1+\Delta\tau(\alpha(1-\tfrac{\beta P_n}{R_n})+N_n)\Big),\\
R_{n+1} &= R_n\Big(1+\Delta\tau(\gamma-\delta N_n-\epsilon P_n)\Big),
\end{aligned}$$

and using $0 \le N_n, P_n \le M$, $m \le R_n \le M$, we estimate from below:

$$\begin{aligned}
1+\Delta\tau\Big(1-\frac{N_n}{R_n}-P_n\Big) &\ge 1-\Delta\tau\Big(\frac{M}{m}+M\Big),\\
1+\Delta\tau\Big(\alpha(1-\frac{\beta P_n}{R_n})+N_n\Big) &\ge 1-\Delta\tau\alpha\beta\frac{M}{m},\\
1+\Delta\tau\Big(\gamma-\delta N_n-\epsilon P_n\Big) &\ge 1-\Delta\tau(\delta M+\epsilon M),
\end{aligned}$$

and each factor is nonnegative under (4.2).

The step-size restriction $\Delta\tau \le \Delta\tau_{\text{pos}}$ guarantees that the discrete map remains biologically well-posed (positive and bounded), preserving numerical artifacts where large steps could artifically drive populations negative or resources below the minimum threshold m.

Remark 4.1. *The bound* (4.2) *is sufficient but not necessary. It ties positivity to the same constants M, m that define the absorbing box $\mathcal{K}(M,m)$. Once the trajectory has entered $\mathcal{K}(M,m)$, the map $\Phi_{\Delta\tau}$ preserves the positive cone for all subsequent steps, provided $\Delta\tau \le \Delta\tau_{\text{pos}}$.*

We show the dissipativity. Define the linear Lyapunov function

$$V(N,P,R) := N + \alpha P + \frac{1}{\gamma}R. \tag{4.3}$$

Because V is linear, the Euler increment satisfies:

$$V_{n+1}-V_n = \Delta\tau\Big[N_n\Big(1-\frac{N_n}{R_n}-P_n\Big)+\alpha(\alpha P_n(1-\tfrac{\beta P_n}{R_n})+N_nP_n)+\frac{1}{\gamma}R_n(\gamma-\delta N_n-\epsilon P_n)\Big].$$

Lemma 4.2 (One-step dissipativity)**.** *There exist constants $A, B > 0$ depending only on $\alpha, \beta, \delta, \epsilon, \gamma$ and on the box $\mathcal{K}(M,m) = \{0 \le N, P \le M,\ m \le R \le M\}$. For all $(N_n, P_n, R_n) \in \mathcal{K}(M,m)$,*

$$V_{n+1} \le (1 - B\Delta\tau)V_n + A\Delta\tau,$$

where $V(N,P,R) := N + \alpha P + \frac{1}{\gamma}R$. In particular, if $\Delta\tau \le \min\{\Delta\tau_{\text{pos}}, B^{-1}\}$, then V_n is uniformly bounded and the orbit of $\Phi_{\Delta\tau}$ enters and remains in a compact subset of $\mathcal{K}(M,m)$.

Proof. Recall the Euler increment for V:

$$V_{n+1} - V_n = \Delta\tau\Big\{N\Big(1 - \frac{N}{R} - P\Big) + \alpha\Big(\alpha P\Big(1 - \frac{\beta P}{R}\Big) + NP\Big) + \frac{1}{\gamma}R(\gamma - \delta N - \epsilon P)\Big\},$$

so, setting $G(N,P,R)$ equal to the brace, we have

$$V_{n+1} - V_n = \Delta\tau\, G(N_n, P_n, R_n).$$

Expanding G and grouping terms gives

$$\begin{aligned} G &= N - \frac{N^2}{R} - NP + \alpha^2 P - \frac{\alpha^2\beta P^2}{R} + \alpha NP + R - \frac{\delta}{\gamma}RN - \frac{\epsilon}{\gamma}RP \\ &= \underbrace{\Big(-\frac{N^2}{R} - \frac{\alpha^2\beta P^2}{R} + (\alpha - 1)NP\Big)}_{\Phi(N,P,R)} + (N + \alpha^2 P + R) \ - \ \frac{\delta}{\gamma}RN - \frac{\epsilon}{\gamma}RP. \end{aligned}$$

All variables lie in the compact box $\mathcal{K}(M,m)$, so $0 \le N, P \le M$, and $m \le R \le M$. Using the elementary bounds

$$-\frac{N^2}{R} \le -\frac{N^2}{M}, \qquad -\frac{\alpha^2\beta P^2}{R} \le -\frac{\alpha^2\beta P^2}{M}, \qquad -\frac{\delta}{\gamma}RN \le -\frac{\delta m}{\gamma}N, \qquad -\frac{\epsilon}{\gamma}RP \le -\frac{\epsilon m}{\gamma}P,$$

we can estimate the quadratic and mixed terms by constants depending on M, m.

Now treat the purely quadratic part $\Phi(N,P,R)$. Fix any constant

$$c_4 > \max\{1,\ \alpha\}.$$

Consider the continuous function

$$\Psi(N,P,R) := \Phi(N,P,R) + c_4(N + \alpha P)$$

on the compact set $\mathcal{K}(M,m)$. By continuity and compactness Ψ attains a maximum; denote

$$C_1 := \max_{(N,P,R)\in\mathcal{K}(M,m)} \Psi(N,P,R) < \infty.$$

Equivalently, for every $(N,P,R) \in \mathcal{K}(M,m)$,

$$\Phi(N,P,R) \le -c_4(N + \alpha P) + C_1.$$

Substituting this bound into the expression for G and dropping the negative terms $-\frac{\delta}{\gamma}RN$ and $-\frac{\epsilon}{\gamma}RP$ yields

$$\begin{aligned} G &\le -c_4(N+\alpha P) + C_1 + N + \alpha^2 P + R \\ &= -(c_4-1)N - \alpha(c_4-\alpha)P + R + C_1. \end{aligned}$$

Set

$$B_1 := c_4 - 1 > 0, \qquad B_2 := c_4 - \alpha > 0.$$

Then

$$G \le -B_1 N - \alpha B_2 P + R + C_1.$$

Choose

$$B \in \Big(0, \min\{B_1, B_2\}\Big].$$

Adding and subtracting the quantity $B(N + \alpha P + \frac{1}{\gamma}R) = BV$, we get

$$G = (G + BN + B\alpha P + B\tfrac{1}{\gamma}R) - BV \le ((B-B_1)N + \alpha(B-B_2)P + (1+\tfrac{B}{\gamma})R + C_1) - BV.$$

By our choice $B \le B_1, B_2$, the coefficients of N and P in the parentheses are nonpositive. Using $0 \le R \le M$, we obtain the uniform bound

$$G \le -BV + \underbrace{((1+\tfrac{B}{\gamma})M + C_1)}_{=:A_0}.$$

Thus, for all $(N,P,R) \in \mathcal{K}(M,m)$,

$$V_{n+1} - V_n = \Delta\tau\, G \le \Delta\tau(-BV_n + A_0),$$

which rearranges to

$$V_{n+1} \le (1 - B\Delta\tau)V_n + A_0\Delta\tau.$$

Setting $A := A_0$ gives the desired inequality.

Finally, if $\Delta\tau \le \min\{\Delta\tau_{\text{pos}}, B^{-1}\}$, then $1 - B\Delta\tau \in [0,1)$ and the discrete inequality yields

$$V_{n+1} \le (1-B\Delta\tau)^{n+1}V_0 + A\Delta\tau\sum_{k=0}^{n}(1-B\Delta\tau)^k \le V_0 + \frac{A}{B}.$$

Hence V_n is uniformly bounded by $V_0 + A/B$ for all n. Because V is a positive linear combination of N, P, R and $\mathcal{K}(M,m)$ is bounded, the uniform bound on V_n, together with the positivity-preserving step-size restriction $\Delta\tau \le \Delta\tau_{\text{pos}}$, implies that the forward orbit enters and remains in a compact subset of $\mathcal{K}(M,m)$. This completes the proof.

Corollary 4.1 (Discrete absorbing set)**.** *Under the hypotheses of Lemma 4.2, there exists $M' > 0$ such that, for all $\Delta\tau \le \min\{\Delta\tau_{\text{pos}}, B^{-1}\}$, the forward orbit of $\Phi_{\Delta\tau}$ enters the box $\mathcal{K}(M',m')$ for some $M' > 0$ (depending on M, m, $\Delta\tau$) and remains there for all subsequent steps.*

We next show stability of the discrete map (4.1).

Theorem 4.1 (Convergence of the discrete map as $\Delta\tau \to 0$)**.** *Let $F : \{(x, y, z) \in \mathbb{R}^3 : x \geq 0, y \geq 0, z > 0\} \to \mathbb{R}^3$ be locally Lipschitz, and let $X(t)$ be the unique solution of the ODE*

$$\dot{X} = F(X), \qquad X(0) = X_0.$$

Let $\{X_n\}_{n\geq 0}$ be generated by the explicit Euler map

$$X_{n+1} = X_n + \Delta\tau\, F(X_n), \qquad X_0 = X(0),$$

and define $t_n = n\Delta\tau$. Then, for any finite $T > 0$, there exists a constant $C_T > 0$ (independent of $\Delta\tau$) such that

$$\max_{0\leq n\leq T/\Delta\tau} \|X(t_n) - X_n\| \leq C_T\, \Delta\tau. \tag{4.4}$$

Hence, the Euler scheme converges to the exact solution with first-order accuracy as $\Delta\tau \to 0$.

Proof. We denote the global error by

$$e_n := X(t_n) - X_n.$$

Let $L > 0$ be a Lipschitz constant for F on a compact set containing $\{X(t) : t \in [0, T]\}$ and all discrete iterates $\{X_n\}$ for $\Delta\tau$ sufficiently small. Then

$$\|F(X) - F(Y)\| \leq L\|X - Y\| \quad \text{for all } X, Y \text{ in this set.}$$

The exact solution satisfies the integral equation

$$X(t_{n+1}) = X(t_n) + \int_{t_n}^{t_{n+1}} F(X(s))\, ds.$$

Subtract and add $\Delta\tau F(X(t_n))$:

$$X(t_{n+1}) = X(t_n) + \Delta\tau F(X(t_n)) + \int_{t_n}^{t_{n+1}} \big[F(X(s)) - F(X(t_n))\big]\, ds.$$

Define the *local truncation error*

$$\tau_{n+1} := \int_{t_n}^{t_{n+1}} [F(X(s)) - F(X(t_n))]\, ds.$$

Since F is Lipschitz and X is continuously differentiable,

$$\|F(X(s)) - F(X(t_n))\| \leq L\|X(s) - X(t_n)\| = L\left\| \int_{t_n}^{s} F(X(r))\, dr \right\| \leq LM|s - t_n|,$$

where $M := \max_{0\leq t\leq T} \|F(X(t))\|$. Hence

$$\|\tau_{n+1}\| \leq \int_{t_n}^{t_{n+1}} LM(s - t_n)\, ds = \frac{1}{2} LM(\Delta\tau)^2.$$

Thus, each local truncation error is $O(\Delta\tau^2)$.

Subtract the discrete update $X_{n+1} = X_n + \Delta\tau F(X_n)$ from the exact step to obtain

$$e_{n+1} = X(t_{n+1}) - X_{n+1} = X(t_n) - X_n + \Delta\tau[F(X(t_n)) - F(X_n)] + \tau_{n+1},$$

or equivalently,

$$e_{n+1} = (I + \Delta\tau A_n)e_n + \tau_{n+1},$$

where A_n is a bounded linear operator satisfying $\|A_n v\| \le L\|v\|$ by the Lipschitz property.

Taking norms and using subadditivity:

$$\|e_{n+1}\| \le (1 + L\Delta\tau)\|e_n\| + C_1(\Delta\tau)^2,$$

where $C_1 = \frac{1}{2}LM$.

Starting from $e_0 = 0$ (since $X_0 = X(0)$), we iterate the above inequality:

$$\|e_n\| \le C_1(\Delta\tau)^2 \sum_{k=0}^{n-1}(1 + L\Delta\tau)^k = C_1(\Delta\tau)^2 \frac{(1 + L\Delta\tau)^n - 1}{L\Delta\tau}.$$

Because $(1 + L\Delta\tau)^n \le e^{Lt_n} \le e^{LT}$ for $t_n \le T$, it follows that

$$\|e_n\| \le \frac{C_1}{L}(e^{LT} - 1)\,\Delta\tau.$$

Setting

$$C_T := \frac{C_1}{L}(e^{LT} - 1) = \frac{M}{2}(e^{LT} - 1)$$

gives the uniform bound

$$\max_{0\le n\le T/\Delta\tau} \|X(t_n) - X_n\| \le C_T\,\Delta\tau.$$

The global error is therefore $O(\Delta\tau)$ as $\Delta\tau \to 0$, demonstrating first-order convergence of the Euler discretization to the continuous ODE solution.

Corollary 4.2 (Numerical–ecological consistency of the discrete model)**.** *Let F and $\Phi_{\Delta\tau}$ be as in Theorem 4.1. Then for any fixed initial data $X_0 = (N_0, P_0, R_0) \in \mathbb{R}^3_{\ge 0}$ with $R_0 > 0$, the iterates of the discrete Euler map*

$$X_{n+1} = \Phi_{\Delta\tau}(X_n)$$

satisfy

$$X_n = X(t_n) + O(\Delta\tau), \qquad t_n = n\Delta\tau,$$

where $X(t)$ is the continuous trajectory of the ODE $\dot{X} = F(X)$. In particular:

(i) the discrete trajectories converge uniformly on bounded time intervals to the continuous ones as $\Delta\tau \to 0$;

(ii) the discrete dynamics thus provide a consistent numerical and biological approximation to the continuous intraguild predation model.

Proof. From Theorem 4.1, $\max_{0\le n\le T/\Delta\tau}\|X(t_n)-X_n\| \le C_T\Delta\tau$. Hence $X_n = X(t_n)+O(\Delta\tau)$ uniformly for $t_n \in [0,T]$. Since the error vanishes linearly with $\Delta\tau$, the discrete map $\Phi_{\Delta\tau}$ converges in phase space to the continuous vector field F. Thus, for sufficiently small time steps, the Euler discretization preserves the qualitative behavior of the original ecological system.

We conclude this section by justifying our choice of the explicit forward Euler schemes, selected primarily for their biological interpretability and algebraic transparency. First, this discretization preserves the fundamental structure of the continuous model: Lemma 4.1 guarantees the preservation of positivity (subject to the derived step-size constraint), while Theorem 4.1 establishes convergence and consistency—properties essential for ensuring ecological validity in simulations. Second, the explicit formulation facilitates the derivation of closed-form positivity and consistency thresholds (Eqs (4.2) and (4.4)), which are often intractable with implicit solvers. Finally, this approach enables a rigorous analysis of discrete dynamical phenomena, including numerical bifurcation absent in the continuous system (Section 4.2), allowing us to characterize the precise stability boundaries of the discrete map.

4.2. Linearization and stability inheritance

Let $X^* = (N^*, P^*, R^*)$ be a fixed point of (4.1) (hence an equilibrium of (2.4)), and $\mathcal{J} := DF(X^*)$ the Jacobian of the ODE right-hand side at X^*. The Jacobian of the Euler map at X^* satisfies

$$D\Phi_{\Delta\tau}(X^*) = I + \Delta\tau J. \tag{4.5}$$

If $\{\lambda_j\}$ are the ODE eigenvalues of $\mathcal{J}$, then the multipliers (discrete eigenvalues) are

$$\mu_j(\Delta\tau) = 1 + \Delta\tau\lambda_j, \qquad j = 1,2,3. \tag{4.6}$$

Proposition 4.1 (Stability inheritance for small $\Delta\tau$)**.** *If $\Re\lambda_j < 0$ for all j, then there exists $\Delta\tau_0 > 0$ such that $|\mu_j(\Delta\tau)| < 1$ for all j and all $\Delta\tau \in (0, \Delta\tau_0]$. Conversely, if some $\Re\lambda_k > 0$, then $|\mu_k(\Delta\tau)| > 1$ for all sufficiently small $\Delta\tau > 0$.*

Proof. Expand $|\mu_j|^2 = |1+\Delta\tau\lambda_j|^2 = 1 + 2\Delta\tau\Re\lambda_j + O(\Delta\tau^2)$.

Let λ denote a (possibly complex) ODE eigenvalue at a fixed point. Solving $|1+\Delta\tau\lambda| = 1$ gives the codimension-1 bifurcation thresholds of the Euler map:

(i) **Fold (saddle-node) of the map**: $\mu = +1$. For Euler, this occurs only if either $\Delta\tau = 0$ or $\lambda = 0$ (the ODE is at a non-hyperbolic equilibrium).

(ii) **Flip (period-doubling)**: $\mu = -1$ for some real $\lambda < 0$,

$$\Delta\tau_{\text{flip}} = -\frac{2}{\lambda}, \quad \lambda \in \mathbb{R}_{<0}. \tag{4.7}$$

For $\Delta\tau > \Delta\tau_{\text{flip}}$, the fixed point of the map loses stability and a period-2 orbit is born generically.

(iii) **Neimark-Sacker (discrete Hopf)**: for a complex conjugate pair $\lambda = a \pm ib$ with $a < 0$,

$$\Delta\tau_{\text{NS}} = \frac{-2a}{a^2+b^2}, \quad |1+\Delta\tau_{\text{NS}}\lambda| = 1. \tag{4.8}$$

Crossing this curve, a smooth invariant closed curve (quasi-periodic oscillation) typically appears.

Remark 4.2 (Which one occurs first?)**.** *At a given ODE-stable equilibrium, the first discrete bifurcation encountered as* $\Delta\tau$ *increases is the smallest positive value among* $\{\Delta\tau_{\text{flip}}, \Delta\tau_{\text{NS}}\}$ *computed from the ODE eigenvalues via* (4.7) *and* (4.8)*.*

At last, we present the AST algorithm, combining algebraic elimination with spectral criteria to locate bifurcation thresholds.

Algorithm: Algebraic–Spectral Thresholding (AST)

Goal: determine equilibria and their stability transitions for the continuous and discrete ecological systems.
Input: model parameters $(\alpha, \beta, \gamma, \delta, \epsilon, \ldots)$ and timestep $\Delta\tau$.
Steps.

(i) **Algebraic elimination.** Eliminate (N^*, P^*) from the steady–state system to obtain a single polynomial equation in R^*,

$$Q(R^*; \gamma) = 0,$$

whose roots correspond to biologically admissible equilibria.

(ii) **Equilibrium counting via discriminant.** Compute the discriminant $\Delta = \text{Disc}(Q)$ to identify the number and type of real roots. The sign $\Delta > 0$ (distinct roots), $\Delta = 0$ (double root), and $\Delta < 0$ (no real root) determine the count of the ODE eigenvalues.

(iii) **Continuous–time stability.** Evaluate the Jacobian $J = DF(P_3)$ at each interior equilibrium and apply the Routh–Hurwitz criteria to its characteristic polynomial

$$\lambda^3 + a_1\lambda^2 + a_2\lambda + a_3 = 0.$$

The inequalities $a_1 > 0$, $a_3 > 0$, and $a_1a_2 > a_3$ identify locally asymptotically stable equilibria of the ODE system.

(iv) **Discrete–time transfer.** Map each continuous eigenvalue λ to the Euler update multiplier $1 + \Delta\tau\,\lambda$. Apply the Schur–Cohn boundary condition

$$|1 + \Delta\tau\,\lambda| = 1,$$

which defines the discrete–time stability boundary in the $(\Delta\tau, \lambda)$ plane. The inequalities $|1 + \Delta\tau\,\lambda_i| < 1$ for all eigenvalues λ_i ensure numerical stability of the Euler discretization.

Output: equilibrium count and stability classification across both continuous and discrete regimes.

5. Stochastic extension

Having established the well-posedness and bifurcation structure of the well-mixed model, we now examine how demographic fluctuations modify these dynamics.

To capture intrinsic demographic fluctuations arising from finite population effects, we extend the deterministic system (2.4) to a stochastic framework. There are different approaches for demographic noise in population dynamics and epidemic models [44–47]. Following the diffusion-approximation approach developed in [48, 49], each reaction channel in (2.4) is regarded as a Poisson event whose intensity equals the corresponding deterministic flux. Aggregating these events and taking the large-population limit yields an Itô SDE that preserves the deterministic drift while adding biologically interpretable demographic noise. On the other hand, this micro-to-macro viewpoint parallels the mean-field program for hybrid PDE–ABM systems, where discrete stochastic switching is coarse-grained to closed PDEs [50].

Let $X_t = (N_t, P_t, R_t)^\top$ denote the state vector. Instead of the nondimensional system (2.4), we construct a demographic-noise-driven intraguild predation model based on the dimensional intraguild model (2.1):

$$\begin{aligned}
\frac{dN}{dt} &= r_1 N\left(1 - \frac{N}{R}\right) - \eta NP,\\
\frac{dP}{dt} &= r_2 P\left(1 - \frac{\beta_d P}{R}\right) + \eta NP,\\
\frac{dR}{dt} &= \rho R(\Gamma - \delta_d N - \epsilon_d P).
\end{aligned}$$

We represent this system as elementary demographic events. Each event produces a small jump Δ_e in (N, P, R) and occurring at intensity $\Lambda_e(X_t)$. We refer to the dimensional parameters in Table 1. The events and intensities are listed in Table 3.

Table 3. Elementary demographic events generating stochastic fluctuations in the intraguild predation model.

Event type	Increment $\Delta_e = (\Delta N, \Delta P, \Delta R)$	Intensity $\Lambda_e(N, P, R)$	Biological interpretation
Prey reproduction	$(+1, 0, 0)$	$r_1 N$	Intrinsic growth
Prey loss due to logistic competition	$(-1, 0, 0)$	$r_1 N^2/R$	Logistic loss
Prey loss and predator growth	$(-1, +1, 0)$	ηNP	Biomass transfer via intraguild predation
Predation growth	$(0, +1, 0)$	$r_2 P$	Intrinsic growth
Predator self-limitation	$(0, -1, 0)$	$r_2\beta_d P^2/R$	Density-dependent predator mortality
Resource growth	$(0, 0, +1)$	$\rho\Gamma R$	Intrinsic resource replenishment
Resource depletion by prey	$(0, 0, -1)$	$\rho\delta_d RN$	Resource consumption by IG-prey
Resource depletion by predator	$(0, 0, -1)$	$\rho\epsilon_d RP$	Resource consumption by IG-predator

Let $N_e(t)$ be the counting process in Table 3 with intensity $\Lambda_e(N_t, P_t, R_t)$. The exact jump representation is

$$dX_t = \sum_e \Lambda_e(X_t)\Delta_e^\top. \tag{5.1}$$

Writing each counting increment via its predictable compensator plus martingale,

$$dN_e(t) = \Lambda_e(N_t, P_t, R_t)\, dt + d\tilde{M}_e(t).$$

In the regime of large populations, approximate $d\tilde{M}_e(t) \approx \sqrt{\Lambda_e(N_t, P_t, R_t)}dB_e(t)$ with independent standard Brownian motions B_e [48]. Then,

$$dX_t = \mu(X_t)\,dt + G(X_t)\,dB_t, \tag{5.2}$$

where $\mu = (f_1, f_2, f_3)^\top$ is the deterministic drift in (2.1), B_t is an 8-dimensional Brownian motion collecting the independent noises, and the diffusion matrix $G(X_t)$ satisfies

$$G(X_t)G(X_t)^\top = \Sigma(X_t) \coloneqq \sum_e \Lambda_e(X_t)\,\Delta_e\,\Delta_e^\top.$$

One admissible G takes the following form:

$$G(N,P,R) = \begin{pmatrix} \sqrt{r_1 N} & -\sqrt{r_1 N^2/R} & -\sqrt{\eta NP} & 0 & 0 & 0 & 0 & 0 \\ 0 & 0 & \sqrt{\eta NP} & \sqrt{r_2 P} & -\sqrt{r_2\beta_d P^2/R} & 0 & 0 & 0 \\ 0 & 0 & 0 & 0 & 0 & \sqrt{\rho\Gamma R} & -\sqrt{\rho\delta_d NR} & -\sqrt{\rho\epsilon_d PR} \end{pmatrix}.$$

Explicitly, the infinitesimal variance–covariance matrix is

$$\Sigma(N,P,R) = \begin{pmatrix} \sigma_N^2 & \sigma_{NP} & 0 \\ \sigma_{NP} & \sigma_P^2 & 0 \\ 0 & 0 & \sigma_R^2 \end{pmatrix},$$

where

$$\begin{aligned} \sigma_N^2 &= r_1 N(1 + N/R) + \eta NP, \\ \sigma_P^2 &= r_2 P(1 + \beta_d P/R) + \eta NP, \\ \sigma_R^2 &= \rho R(\Gamma + \delta_d N + \epsilon_d P), \\ \sigma_{NP} &= -\eta NP. \end{aligned}$$

Here σ_{NP} encodes the negative covariance between prey and predator fluctuations due to coupled predation events.

Collecting terms, the stochastic Leslie–Gower intraguild predation model reads compactly as

$$dX_t = \mu(X_t)\,dt + G(X_t)\,dB_t. \tag{5.3}$$

Writing explicitly,

$$\begin{cases} dN_t = \left[r_1 N_t(1 - N_t/R_t) - \eta N_t P_t\right]dt + \sqrt{r_1 N_t}\,dB_t^1 - \sqrt{r_1 N_t^2/R_t}\,dB_t^2 - \sqrt{\eta N_t P_t}\,dB_t^3, \\ dP_t = \left[r_2 P_t(1 - \beta_d P_t/R_t) + \eta N_t P_t\right]dt + \sqrt{\eta N_t P_t}\,dB_t^3 + \sqrt{r_2 P_t}\,dB_t^4 - \sqrt{r_2\beta_d P_t^2/R_t}\,dB_t^5, \\ dR_t = \rho R_t(\Gamma - \delta_d N_t - \epsilon_d P_t)\,dt + \sqrt{\rho\Gamma R_t}\,dB_t^6 - \sqrt{\rho\delta_d N_t R_t}\,dB_t^7 - \sqrt{\rho\epsilon_d P_t R_t}\,dB_t^8, \end{cases} \tag{5.4}$$

where the Brownian motions $\{B_i\}$ are mutually independent. (5.4) reduces to the deterministic model (2.1) in the zero-noise limit. We can check that the joint probability density function of (5.4) is a solution of the following multivariate forward Kolmogorov differential equation:

$$\frac{\partial p(x,t)}{\partial t} = \frac{1}{2}\sum_{i,j=1}^{3}\frac{\partial^2}{\partial x_i \partial x_j}\Big[p(x,t)\sum_{l=1}^{3} S_{il}S_{jl}\Big] - \sum_{i=1}^{3}\frac{\partial[p(x,t)\mu_i]}{\partial x_i}, \tag{5.5}$$

where $S_{ij} \equiv S_{ij}(x,t)$ and $\mu_i \equiv \mu_i(x,t)$. Here, S is the positive semidefinite square root of Σ.

System (5.4) captures intrinsic demographic fluctuations in prey–predator–resource interactions. Predation events introduce negatively correlated noise between N_t and P_t, while resource variability adds multiplicative noise modulated by the total biomass. The deterministic bifurcation structure persists in the mean field, but stochastic trajectories exhibit finite-size fluctuations around equilibria and may transiently explore alternative basins of attraction. This stochastic framework thus bridges deterministic intraguild predation theory with demographic variability observed in ecological and microbial populations.

6. Numerical simulations and parameter regimes

6.1. Bifurcation structure and regimes

We now illustrate the analytical results of Section 3 by direct numerical integration of (2.4) under six representative parameter regimes. Each case corresponds to one of the theoretical scenarios in our equilibrium classification (single equilibrium, two equilibria, double equilibrium, or no equilibrium). The parameter sets are listed below, and the corresponding dynamics are shown in Figure 1. All simulations were performed in MATLAB using `ode45` with relative tolerance `RelTol` $= 10^{-9}$ and absolute tolerance `AbsTol` $= 10^{-12}$, starting from $(N(0), P(0), R(0)) = (0.5, 0.5, 0.5)$.

Scenario 1: $\beta\delta \le \epsilon$ and $\gamma < \epsilon$:

$$\alpha = 1, \quad \beta = 2, \quad \delta = 0.5, \quad \epsilon = 1, \quad \gamma = 0.05, \quad \gamma_1^+ = 1.$$

Scenario 2: $\beta\delta > \epsilon$ and $\gamma \le \epsilon$:

$$\alpha = 1, \quad \beta = 2, \quad \delta = 0.5, \quad \epsilon = 0.2, \quad \gamma = 0.2, \quad \gamma_1^+ = 0.3.$$

Scenario 3: $\beta\delta > \epsilon$ and $\epsilon < \gamma < \gamma_1^+$:

$$\alpha = 1, \quad \beta = 2, \quad \delta = 0.5, \quad \epsilon = 0.2, \quad \gamma = 0.24, \quad \gamma_1^+ = 0.3.$$

Scenario 4: $\beta\delta > \epsilon$ and $\gamma = \gamma_1^+$:

$$\alpha = 1, \quad \beta = 2, \quad \delta = 0.5, \quad \epsilon = 0.2, \quad \gamma = 0.3, \quad \gamma_1^+ = 0.3.$$

Scenario 5: $\beta\delta \le \epsilon$ and $\gamma \ge \epsilon$:

$$\alpha = 1, \quad \beta = 2, \quad \delta = 0.5, \quad \epsilon = 1, \quad \gamma = 2, \quad \gamma_1^+ = 1.$$

Scenario 6: $\beta\delta > \epsilon$ and $\gamma > \gamma_1^+$:

$$\alpha = 1, \quad \beta = 2, \quad \delta = 0.5, \quad \epsilon = 0.2, \quad \gamma = 0.5, \quad \gamma_1^+ = 0.3.$$

For Scenarios 1–2, the trajectories converge to a unique positive equilibrium, while in Scenario 3, two equilibria exist and trajectories converge to one of them. Scenario 4 corresponds to the degenerate case $\gamma = \gamma_1^+$, where the Jacobian possesses one zero eigenvalue, indicating the saddle–node bifurcation predicted analytically. For Scenarios 5 and 6, no positive equilibrium exists, and the IG-prey N collapses to extinction, leaving the coexistence of the IG-predator and the resource when $\gamma > \epsilon$.

Figure 1(a) displays the time series of $(N(t), P(t), R(t))$, showing convergence to the boundary equilibrium $\mathcal{E}_2$ or stable coexistence state $\mathcal{E}_3$ depending on parameters. The corresponding phase portraits in Figure 1(b) reveal the geometric nature of each attractor and bifurcation. Table 4 summarizes the computed equilibria and Jacobian spectra from the MATLAB simulations, providing quantitative verification of the theoretical results.

Table 4. Numerical equilibria and Jacobian eigenvalues of system (2.4) for the six parameter regimes shown in Figure 1. A dash indicates that no positive equilibrium exists (trajectories approach boundary equilibria).

Scenario	(N^*, P^*, R^*)	spec = $(\lambda_1, \lambda_2, \lambda_3)$	Equilibrium type	Qualitative outcome
1	(0.0482, 0.0259, 0.0494)	$(-0.0533, -0.9486, -1.0203)$	Stable node	Stable coexistence
2	(0.2963, 0.2593, 0.4000)	$(-0.1720, -0.9325 \pm 0.1537i)$	Stable focus	Damped oscillations
3	(0.3398, 0.3505, 0.5232)	$(-0.1606, -0.9144 \pm 0.2526i)$	Stable focus	Damped oscillations
4	(0.3333, 0.6667, 1.0000)	$(0, -0.8333 \pm 0.4534i)$	Saddle–node (degenerate)	Bifurcation threshold
5	—	—	No positive eq.	To $\mathcal{E}_2$ when $\gamma > \epsilon$
6	—	—	No positive eq.	To $\mathcal{E}_2$ when $\gamma > \epsilon$

To visualize how the number of positive equilibria changes across parameter space, we conducted a systematic numerical sweep in the enrichment parameter γ. We then generated two-dimensional regime maps in the (γ, ϵ) and (γ, β) planes. All simulations use the nondimensional Leslie–Gower intraguild predation model (2.4) with baseline parameters $\alpha = 1, \beta = 2, \delta = 0.5$, and default $\epsilon = 0.2$ unless otherwise specified.

To explore the interplay between γ and other parameters, we constructed two-dimensional maps by classifying each point in parameter space according to the number of positive equilibria:

$$0 : \text{predator-only equilibrium},$$

$$1 : \text{one positive coexistence equilibrium},$$

$$2 : \text{two positive coexistence equilibria}.$$

For each grid point, the classification was determined analytically using the equilibrium condition (3.1).

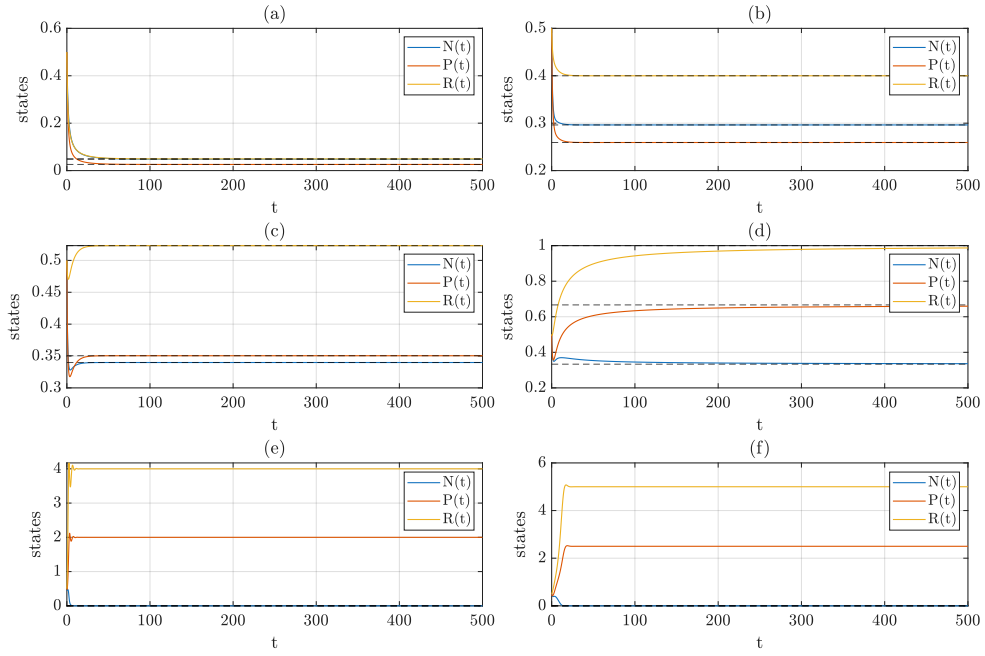

(a) Time series of $(N(t), P(t), R(t))$ for the six parameter regimes. Panels (a)–(f) correspond to Scenarios 1–6. Dashed lines denote equilibrium values (N^*, P^*, R^*).

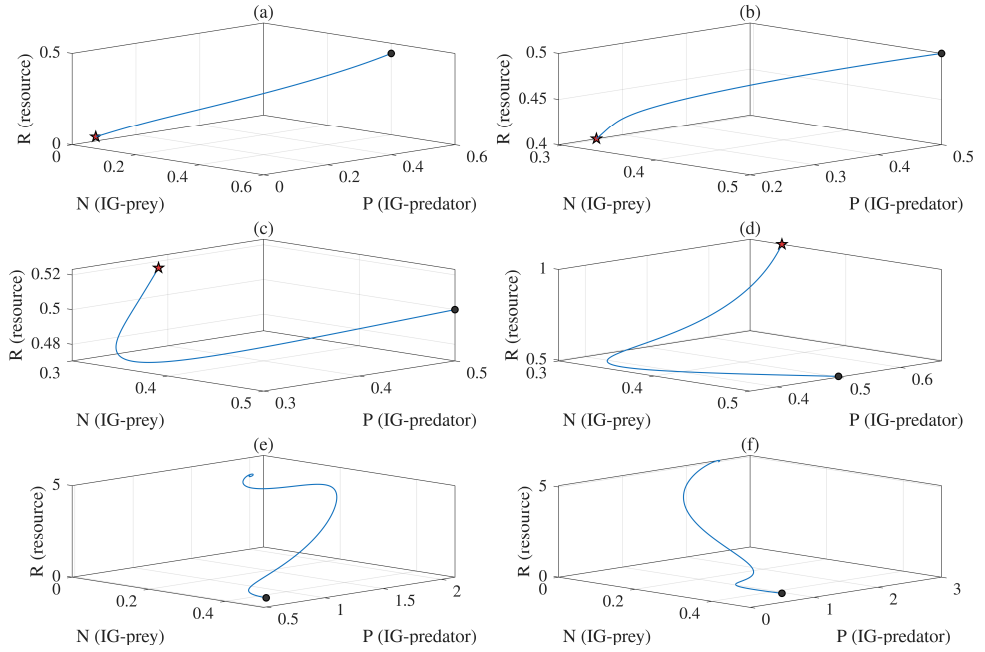

(b) Three-dimensional phase portraits of the trajectories in Figure 1(a). Positive equilibria are shown as red pentagrams and initial states as black circles. Panels (a)–(f) correspond to Scenarios 1–6.

Figure 1. Numerical dynamics of the nondimensional Leslie–Gower intraguild predation model (2.4) under six representative parameter regimes. Panels (a)–(c) show convergence to a stable coexistence equilibrium; (d) corresponds to the saddle–node bifurcation point; (e)–(f) exhibit extinction of the IG-prey species when $\gamma = 0.5 > \epsilon = 0.2$.

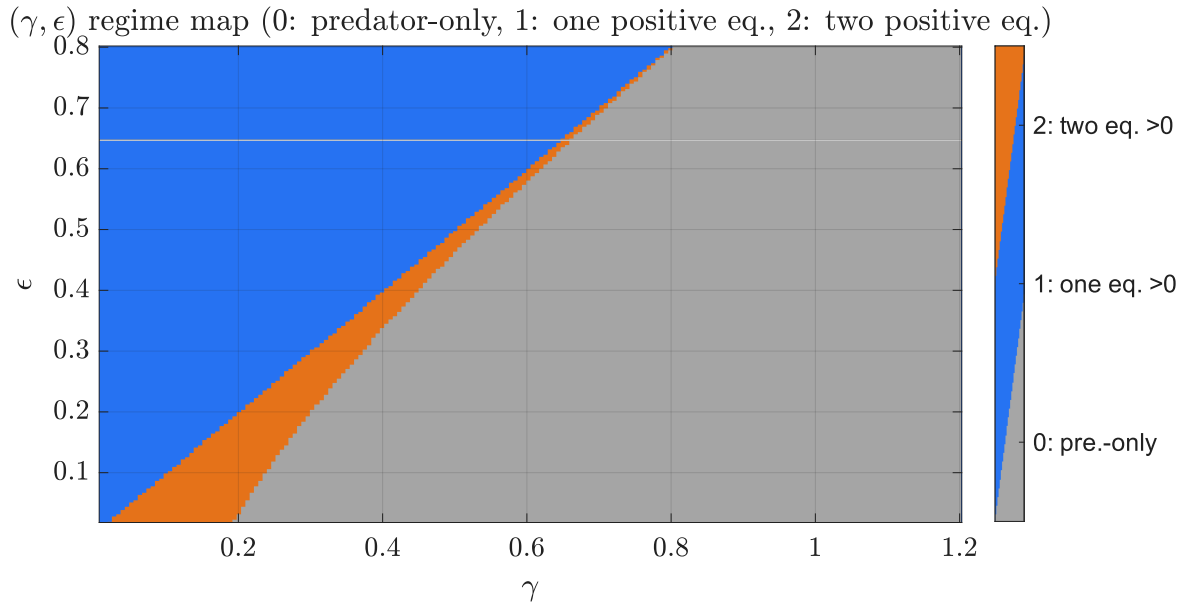

(a) (γ, ϵ)-plane classification: 0 = predator-only (gray), 1 = one positive equilibrium (blue), 2 = two positive equilibria (orange).

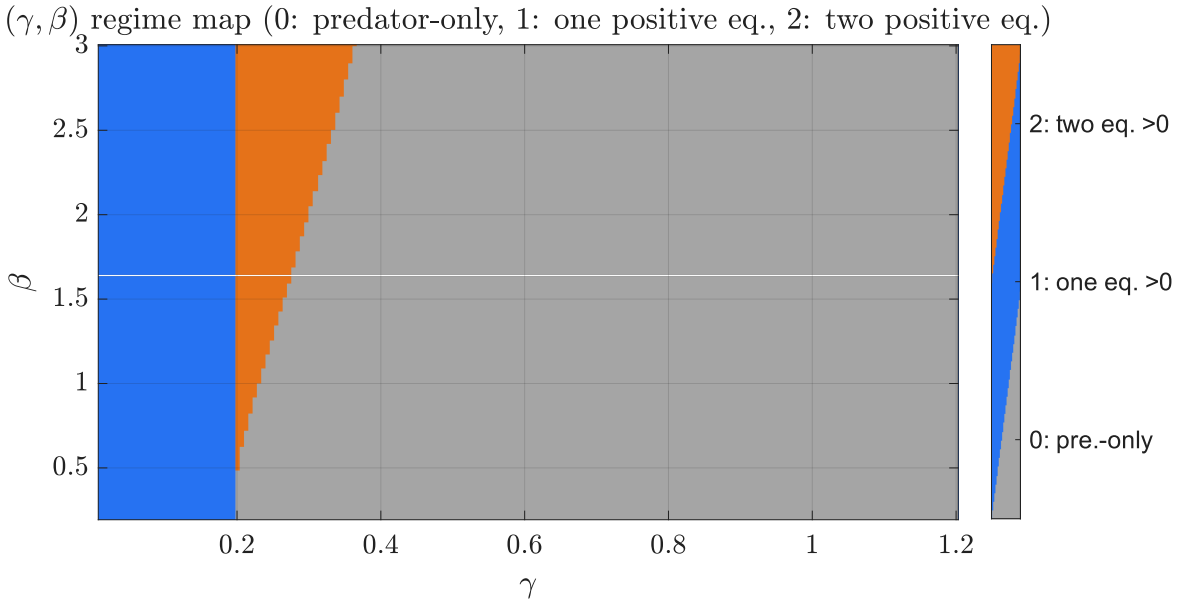

(b) (γ, β)-plane classification for fixed $\epsilon = 0.2$. Colors as in (a).

Figure 2. Regime maps of the equilibrium structure for the Leslie–Gower intraguild predation model. (a) Varying enrichment γ and resource consumption rate ϵ. (b) Varying enrichment γ and predator–prey interaction ratio β. Regions with two interior equilibria (orange) correspond to bistability between coexistence and predator-only states, bounded by the saddle–node curve $\gamma = \gamma_{SN}(\epsilon, \beta)$.

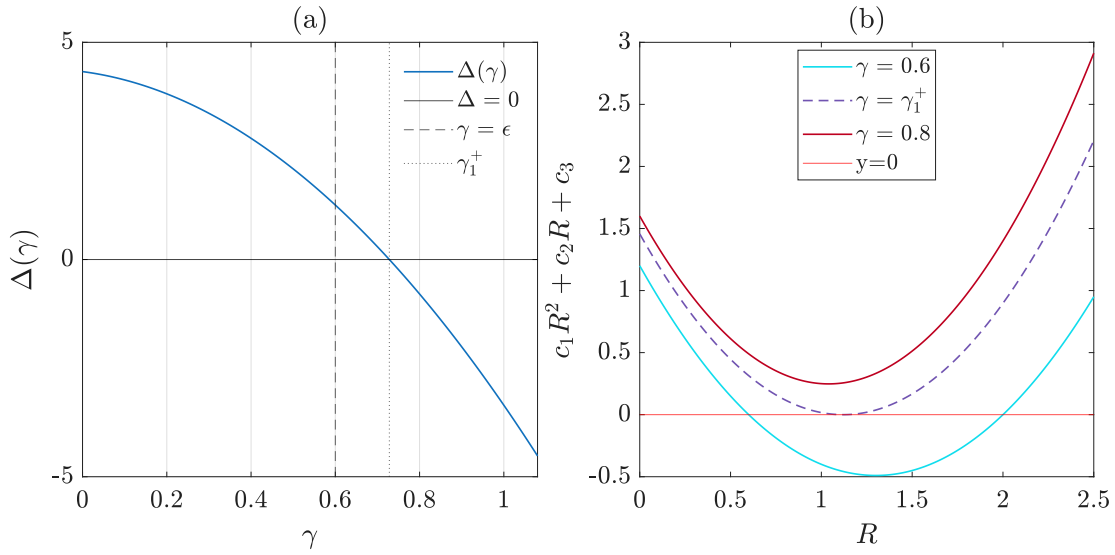

Figure 3. The discriminant $\Delta = \Delta(\gamma)$ and the quadratic relation in (3.1) indicating the number of interior equilibria. (a) Discriminant as a function of γ. (b) The quadratic function $c_1R^2 + c_2R + c_3$ vs. R across $\gamma \in \{0.6, \gamma_1^+, 0.8\}$. Parameters: $\alpha = 0.8, \beta = 2, \delta = 1, \epsilon = 0.6$. Under this parameter setting, $\gamma_1^- = -0.9283 < 0$ and $\gamma_1^+ = 0.7283$.

As expected, a single positive equilibrium exists for $\gamma < \epsilon$. Two coexistence equilibria appear for $\epsilon < \gamma < \gamma_1(\epsilon, \gamma)$. No positive equilibria remain for $\gamma > \gamma_1^+(\epsilon, \gamma)$, where $\gamma_1^+ = \gamma_1^+(\epsilon, \gamma)$ is the analytically predicted saddle–node bifurcation threshold. The predator-only boundary equilibrium $\mathcal{E}_2 = (0, \gamma/\epsilon, \beta\gamma/\epsilon)$ is stable for $\gamma > \epsilon$, confirming the transcritical transition between the coexistence and predator-only states.

Figure 2(a) shows the (γ, ϵ) diagram obtained for fixed $\alpha = 1, \beta = 2, \delta = 0.5$. The curve $\gamma = \epsilon$ separates the one-equilibrium region (Class 1) from the two-equilibrium zone (Class 2). A narrow wedge, $\epsilon < \gamma < \gamma_1^+(\epsilon)$, corresponds to the two-equilibrium zone (Class 2), where two positive equilibria exist simultaneously. As ϵ increases, this wedge shrinks and eventually disappears once $\beta\delta \leq \epsilon$, consistent with Lemma 3.1.

Figure 2(b) shows the analogous (γ, β) map with fixed $\epsilon = 0.2$. Here, increasing β enlarges the two-equilibrium domain, since larger β enhances the threshold γ_1^+ under our fixed parameter set $(\alpha, \delta, \epsilon) = (1, 0.5, 0.2)$. Both diagrams agree quantitatively with the analytical bifurcation surfaces predicted by the discriminant condition of (3.1).

Figure 3 illustrates the discriminant and the quadratic function $y(R) = c_1R^2 + c_2R + c_3$ in (3.1). The two eigenvalues for $\Delta(\gamma)$ are $\gamma_1^- = -0.9283$ and $\gamma_1^+ = 0.7283$. $\beta\delta = 2 > \delta = 0.6$, so Corollary 3.1 predicts that there are 2, 1, and 0 interior eigenvalues when, respectively, $\epsilon < \gamma < \gamma_1^+$, $\gamma = \gamma_1^+$, and $\gamma > \gamma_1^+$. Figure 3(a) shows that $\Delta = \Delta(\gamma)$ has a positive zero $\gamma = \gamma_1^+$. Figure 3(b) validates the theoretical predictions about the number of positive zeros of $y(R) = c_1R^2 + c_2R + c_3$, which is the same as the number of interior equilibria.

6.2. Discrete bifurcation

We next perform a systematic numerical search to identify parameter regimes where the discrete-time Euler map of system (2.4) exhibits qualitatively distinct local bifurcations. Using Latin hypercube sampling of 20,000 parameter combinations $(\alpha, \beta, \gamma, \delta, \varepsilon) \in [10^{-3}, 4]^5$ and scanning $\Delta\tau \in [10^{-4}, 2]$, we detect three canonical bifurcation types of the discrete map $\Phi(X; \Delta\tau)$. A fold (saddle–node) bifurcation occurs when one multiplier crosses $+1$. A flip (period–doubling) bifurcation occurs when one multiplier crosses -1. A Neimark–Sacker (discrete Hopf) bifurcation occurs when a complex-conjugate pair crosses the unit circle. The corresponding parameter sets automatically identified by our MATLAB routine are

$$\text{fold: } (\alpha, \beta, \gamma, \delta, \epsilon, \Delta\tau) = (1.679,\ 1.771,\ 3.886,\ 0.8264,\ 3.89,\ 0.01616),$$

$$\text{flip: } (\alpha, \beta, \gamma, \delta, \epsilon, \Delta\tau) = (2.304,\ 1.909,\ 0.2067,\ 0.4913,\ 2.521,\ 0.8916),$$

$$\text{Neimark–Sacker: } (\alpha, \beta, \gamma, \delta, \epsilon, \Delta\tau) = (1.011,\ 1.635,\ 3.174,\ 3.673,\ 3.708,\ 0.4017).$$

For each bifurcation, we perform a local continuation in the bifurcation parameter γ around the critical value and track the equilibrium (R^*, N^*, P^*) together with the corresponding eigenvalue moduli $|\mu_i|$. As shown in Figure 4, the computed bifurcation diagrams illustrate the distinct multiplier crossings that characterize the fold, flip, and Neimark–Sacker transitions, respectively.

We now illustrate the fold (saddle–node) bifurcation identified in the parameter search (Figure 5). Using the parameter set

$$(\alpha, \beta, \gamma_0, \delta, \epsilon, \Delta\tau) = (1.679,\ 1.771,\ 3.886,\ 0.8264,\ 3.89,\ 0.01616),$$

a local continuation procedure refines the bifurcation value to $\gamma_0 = 3.88967$. The slight discrepancy from the search result (3.886) arises from the numerical tolerance imposed when detecting the critical eigenvalue $\mu = 1$. The corresponding ODE eigenvalue satisfies $\lambda \approx 0$, confirming that the discrete map undergoes a fold bifurcation. Notably, we observe that $\gamma_0 \approx \epsilon$. Since the condition $\beta\delta \leq \epsilon$ holds, Corollary 3.1 predicts that the system admits a single interior equilibrium when $\gamma < \epsilon$ and none when $\gamma \geq \epsilon$. This analytical criterion therefore explains why ϵ acts as the bifurcation threshold for γ and clarifies the observed coincidence $\gamma_0 \approx \epsilon$.

We next vary the bifurcation parameter γ around the critical value γ_0. For $\gamma = 3.8797 < \gamma_0$, the system possesses a stable interior equilibrium

$$(N^*, P^*, R^*) \approx (0.0074,\ 0.9958,\ 1.7557),$$

whereas for $\gamma = 3.8997 > \gamma_0$, no equilibrium persists. At the critical point $\gamma = \gamma_0$, the equilibrium disappears, and the discrete-time Jacobian acquires a unit multiplier ($\mu = 1$). Figure 5 corroborates this behavior: as γ crosses γ_0, the spectral radius of the map satisfies $\rho(D\Phi) = 1$, indicating the loss of stability and the disappearance of the fixed point.

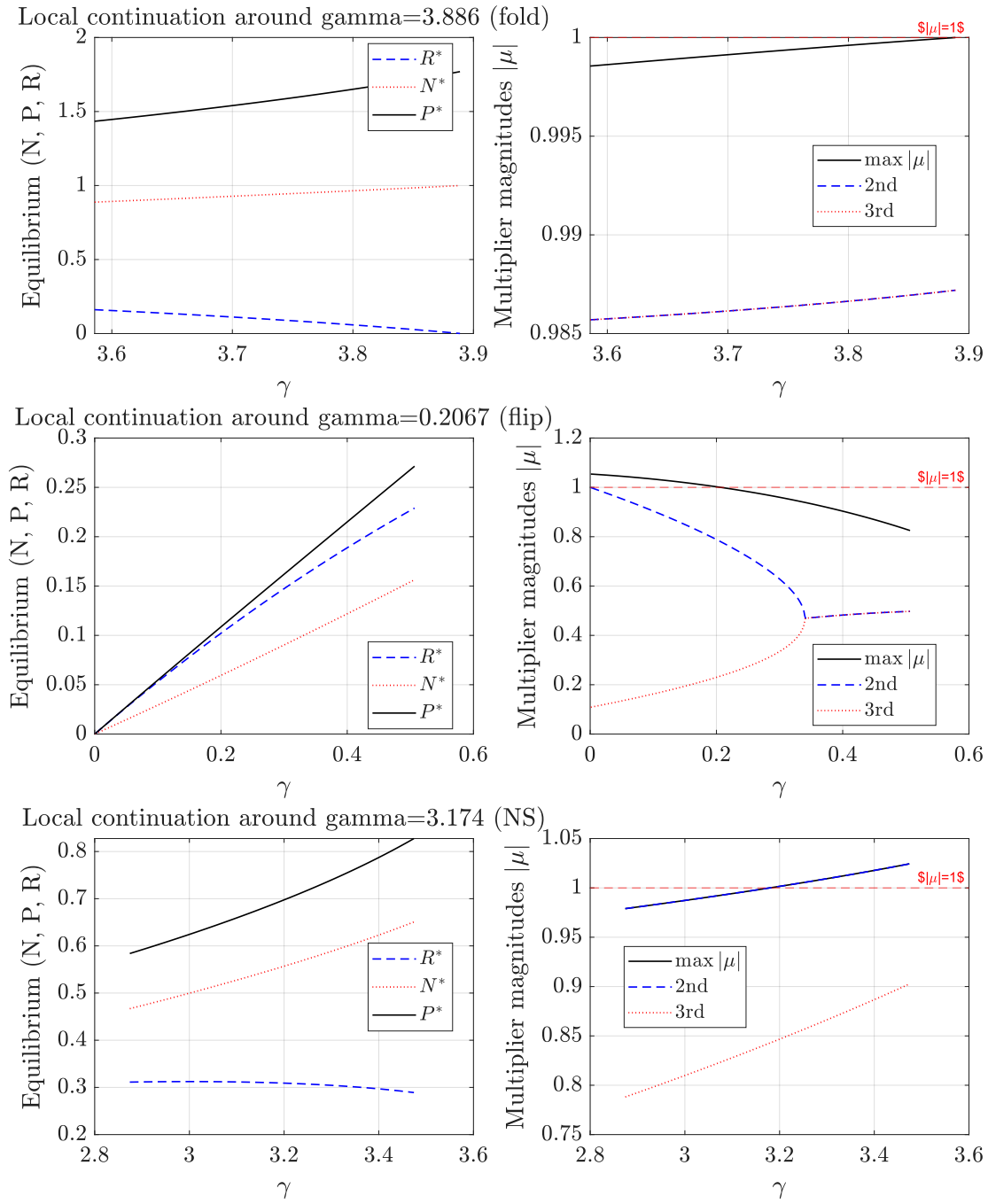

Figure 4. Numerical detection and local continuation of the three discrete-time bifurcations of the Euler map $\Phi(X;\Delta\tau)$. Each row corresponds to one bifurcation type identified by the automated parameter sweep: (**a,b**) fold (saddle–node) with a multiplier crossing +1, (**c,d**) flip (period–doubling) with a multiplier crossing −1, and (**e,f**) Neimark–Sacker with a complex pair crossing the unit circle. Left panels show equilibrium components (R^*, N^*, P^*) versus γ; right panels plot the corresponding multiplier moduli $|\mu_i|$, where $|\mu| = 1$ (dashed line) marks the discrete stability boundary.

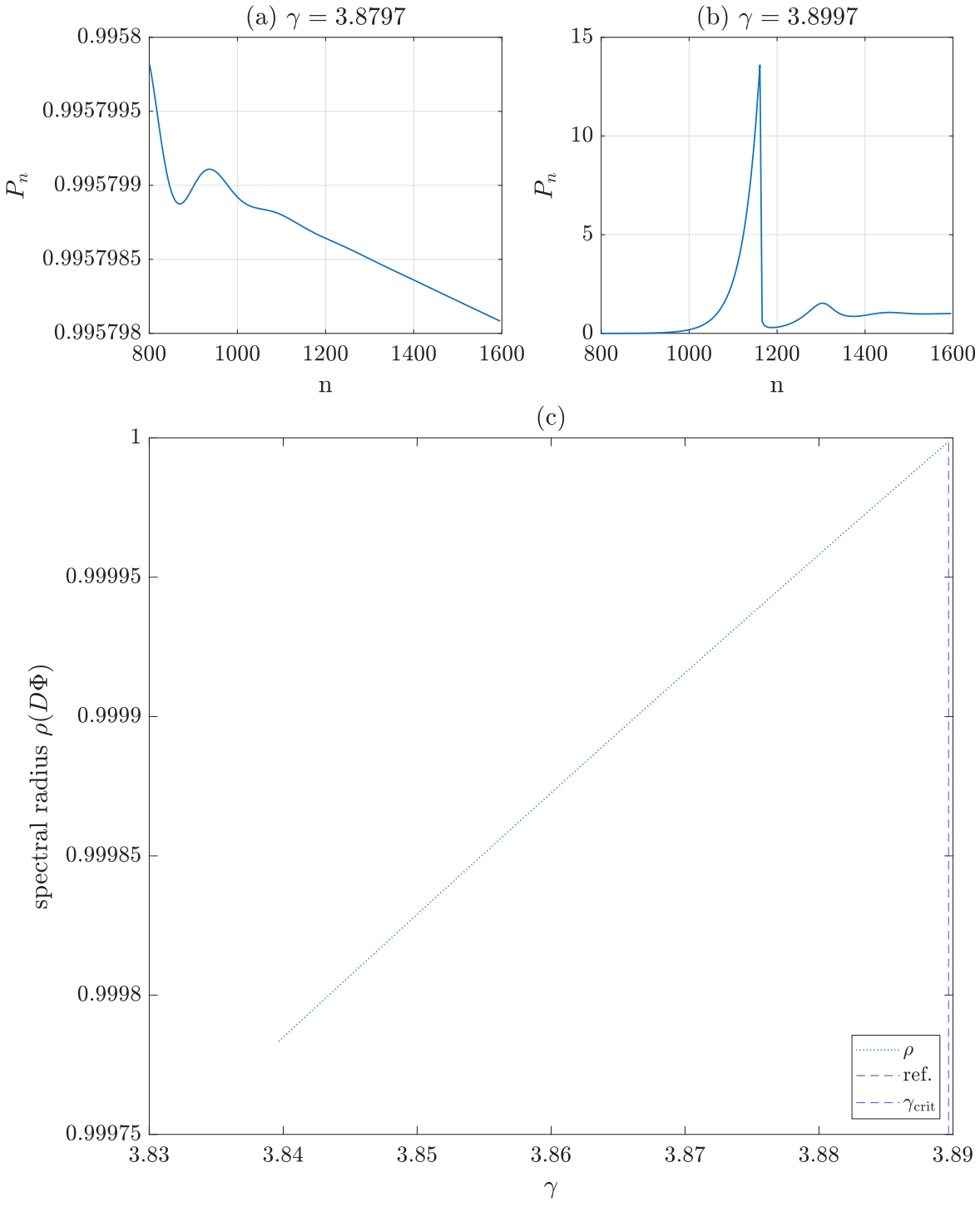

Figure 5. Numerical illustration of the fold bifurcation for the forward-Euler map. (**a**,**b**) Time series of P_n for γ below and above the critical value $\gamma_0 = 3.88967$, showing the disappearance of the equilibrium as γ crosses γ_0. (**c**) Spectral radius $\rho(D\Phi)$ as a function of γ, with $\rho = 1$ (dashed line) and γ_{crit} (vertical line) marking the fold point where the unit multiplier ($\mu = 1$) emerges.

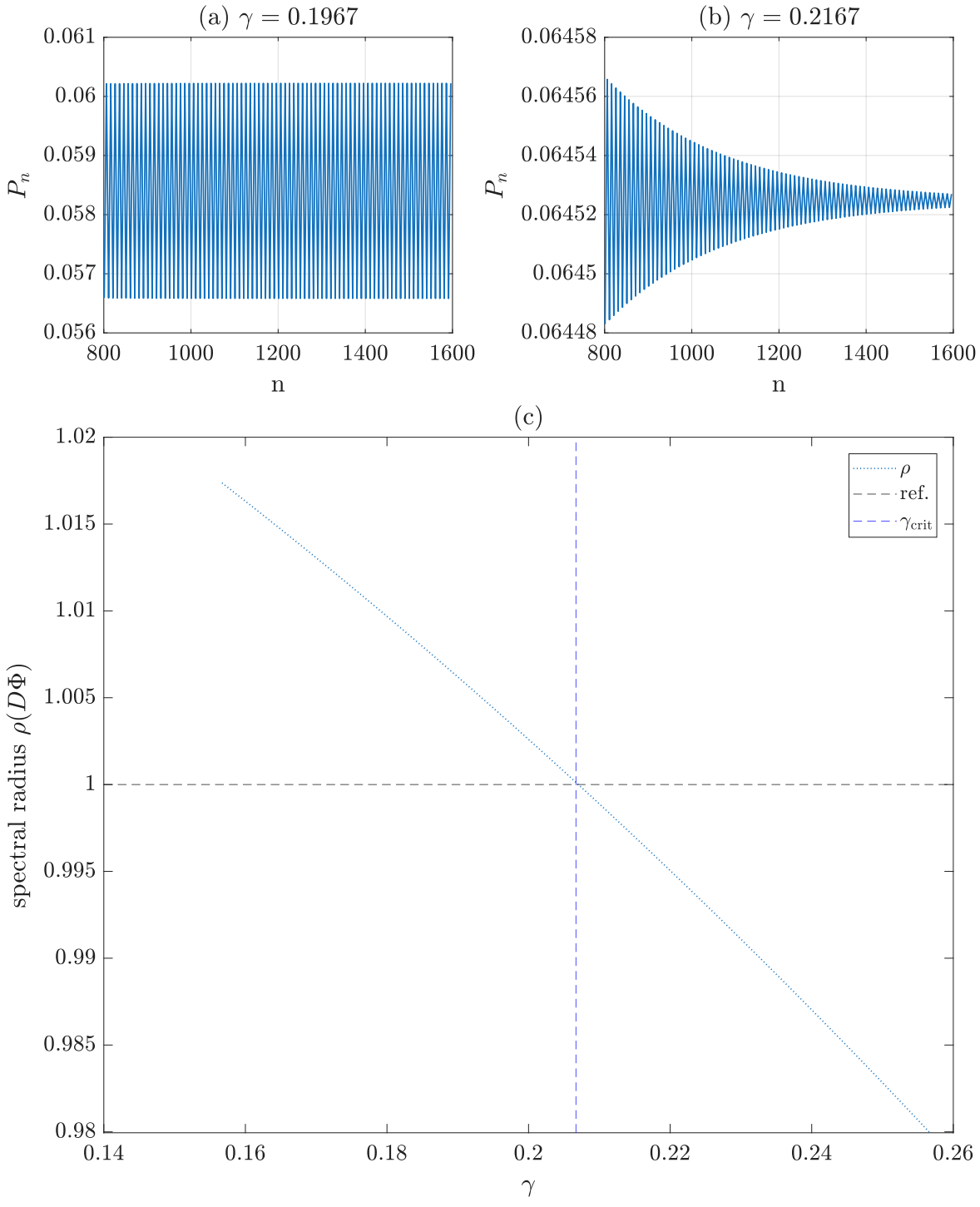

Figure 6. Numerical illustration of the flip (period-doubling) bifurcation as the bifurcation parameter γ crosses the critical value $\gamma_0 = 0.2067$. (**a**,**b**) Time series of P_n obtained from iterating the Euler map with γ slightly below and above γ_0, respectively, showing the transition from a stable period-two oscillation to a stable fixed point. (**c**) Spectral radius $\rho(D\Phi)$ as a function of γ, with $\rho = 1$ (dashed line) marking the stability boundary and γ_{crit} (vertical line) indicating the crossing where the multiplier passes through $\mu = -1$.

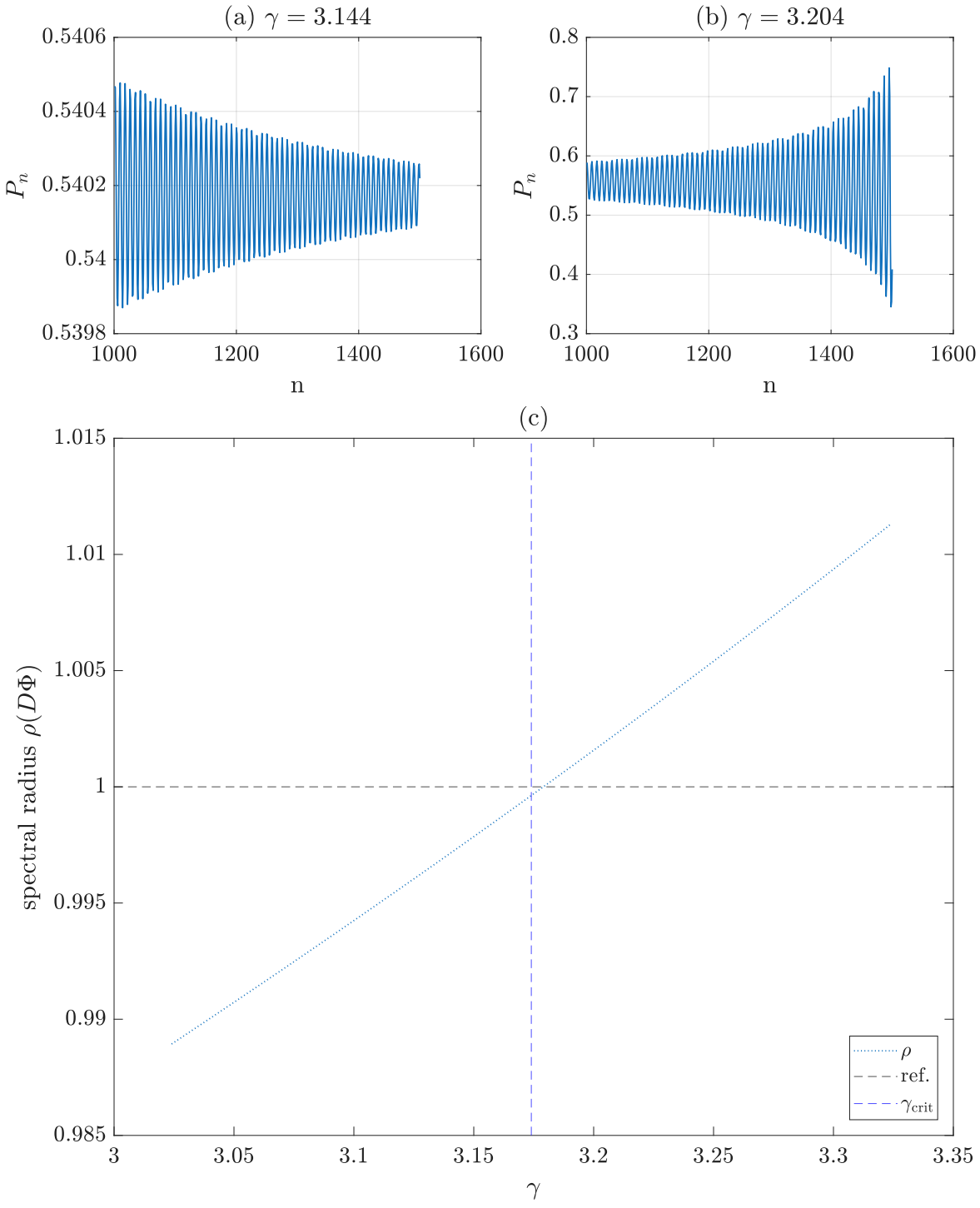

Figure 7. Numerical illustration of the Neimark–Sacker (discrete Hopf) bifurcation for the forward-Euler map. (**a**,**b**) Time series of P_n for γ slightly below and above the critical value $\gamma_0 = 3.174$, showing the transition from a stable equilibrium to small-amplitude quasiperiodic oscillations. (**c**) Spectral radius $\rho(D\Phi)$ as a function of γ, with $\rho = 1$ (dashed line) marking the stability boundary and γ_{crit} (vertical line) indicating the crossing of a complex conjugate pair of multipliers through the unit circle.

We next examine the local dynamics near the flip (period-doubling) bifurcation identified in Figure 4. Using the parameter set obtained from the automated search,

$$(\alpha, \beta, \gamma_0, \delta, \epsilon, \Delta\tau) = (2.304,\ 1.909,\ 0.2067,\ 0.4913,\ 2.521,\ 0.8916),$$

we vary the feedback parameter γ slightly below and above its critical value γ_0. For $\gamma = 0.2167 > \gamma_0$, the Euler map admits a stable fixed point

$$(N^*, P^*, R^*) \approx (0.10998,\ 0.06452,\ 0.11757),$$

whose multipliers are approximately $(-0.9963,\ 0.2435,\ 0.7664)$. In contrast, for $\gamma = 0.1967 < \gamma_0$, the leading multiplier crosses the unit circle at $\mu \approx -1.0038$. The P-component of the map oscillates between 0.057 and 0.060 on successive iterations, signaling the onset of a period-two orbit. As γ decreases further, the spectral radius exceeds 1, confirming the loss of stability of the fixed point.

Figure 6 visualizes this transition. As γ passes through γ_0, the spectral radius of the discrete Jacobian satisfies $\rho(D\Phi) = 1$ at the critical point. This corresponds to a characteristic eigenvalue crossing at $\mu = -1$, which defines the flip (period-doubling) bifurcation.

Finally, we illustrate the Neimark–Sacker (discrete Hopf) bifurcation using the parameter set

$$(\alpha, \beta, \gamma_0, \delta, \epsilon, \Delta\tau) = (1.011,\ 1.635,\ 3.174,\ 3.673,\ 3.708,\ 0.4017),$$

and vary the bifurcation parameter γ slightly below and above the critical value γ_0. For $\gamma = 3.144 < \gamma_0$, the system converges to the steady state

$$(N^*, P^*, R^*) \approx (0.3107,\ 0.5401,\ 0.6756),$$

with a pair of complex conjugate multipliers $\mu_{2,3} = 0.7242 \pm 0.6859i$ lying strictly inside the unit circle, indicating local stability. When γ increases to $3.204 > \gamma_0$, these multipliers satisfy $|\mu_{2,3}| > 1$, causing the fixed point to lose stability and generate a quasiperiodic oscillation. This marks the onset of a Neimark–Sacker bifurcation—the discrete analogue of a Hopf bifurcation in continuous time.

Figure 7 visualizes this transition. As γ passes through γ_0, the time series of P_n evolves from steady convergence to persistent oscillations. At the critical point, the spectral radius $\rho(D\Phi)$ reaches unity, consistent with the bifurcation condition $|\mu| = 1$ for a complex conjugate pair of multipliers.

The numerical simulations confirm the analytical predictions of the model, capturing the spectrum of equilibrium behaviors and bifurcation phenomena across parameter regimes. Continuous-time integrations reproduce the coexistence, saddle-node bifurcation, and extinction scenarios, while discrete-time analyses reveal classical fold, flip, and Neimark–Sacker bifurcations. Together, these results demonstrate the consistency between theory and computation, and highlight the rich dynamical structures inherent in intraguild predation systems.

7. Discussion and conclusions

We developed a discrete–time and stochastic framework for the intraguild predation system. This extends the continuous–time bifurcation theory of Yao and Yuan [33] to a fully explicit and computationally verifiable setting. The proposed formulation captures the essential biological

constraints of nonnegativity and boundedness while enabling rigorous stability and bifurcation analysis directly in the discrete map. By combining algebraic–spectral criteria with dissipativity proofs and stochastic extensions, the approach establishes a transparent correspondence between deterministic bifurcations, numerical thresholds, and demographic fluctuations.

Our main contributions can be summarized as follows:

(i) Discrete-map formulation and dissipativity. We derive the forward–Euler map associated with the continuous ODE system. We then prove positivity, boundedness, and existence of an absorbing set under an explicit stepsize bound, ensuring dynamical consistency between discrete and continuous regimes.

(ii) Algebraic–spectral threshold algorithm. A closed–form algorithm detects equilibrium transitions and classifies local dynamics by combining algebraic coefficients and spectral radii of the Jacobian. This provides computable bifurcation thresholds—including saddle–node, flip, and Neimark–Sacker loci—with guaranteed correspondence to the ODE's spectral conditions.

(iii) Demographic noise extension. Incorporating multiplicative demographic fluctuations transforms the deterministic map into a system of Itô–SDEs. The corresponding Fokker–Planck dynamics show how finite-population noise modulates variability near bifurcation thresholds.

(iv) Numerical verification. Extensive simulations confirm parameter space classification (Corollary 3.1) and reproduce predicted transitions. They also visualize the correspondence between algebraic bifurcation conditions and qualitative dynamical behavior.

Beyond their theoretical interest, our mathematical results offer concrete predictive tools for ecosystem management, particularly for intraguild predation systems like the Lake Kinneret food web. First, the derivation of explicit algebraic thresholds (e.g., the saddle-node value γ_1^+) translates abstract stability conditions into quantifiable tipping points. Ecologically, this implies that nutrient enrichment (γ) cannot be increased indefinitely; crossing the calculated threshold triggers a catastrophic transition from coexistence to species exclusion (prey collapse), rather than a gradual decline. Second, the detection of Neimark–Sacker and flip bifurcations in the discrete domain highlights a distinct vulnerability for species with non-overlapping generations (seasonal breeders). Unlike continuous breeders, these populations are prone to overshoot dynamics driven by reproductive time lags, leading to high-amplitude oscillations that increase the risk of stochastic extinction during population troughs. Finally, the stochastic extension demonstrates that demographic noise is not merely uncertainty on the dynamics but a suppressor of population extinction, supporting the argument that environmental noise, rather than demographic noise, is the main driver of population extinction.

The resulting framework unifies analytical, stochastic, and computational perspectives within a single discrete-time model. Methodologically, the AST algorithm offers a distinct improvement over purely numerical bifurcation analyses. By engaging the algebraic structure of the system (using discriminants and trace), it ensures that the detected tipping points—such as the saddle-node and Neimark–Sacker bifurcations—are mathematically exact features of the model rather than artifacts of numerical approximation or step-size sensitivity.

7.1. Limitations and future directions

While the AST algorithm provides exact thresholds for the current IGP system, its applicability to general ecological models warrants discussion. A primary limitation is the algebraic complexity associated with higher-dimensional systems. For food webs with $N \geq 5$ species, the characteristic polynomials of the Jacobian matrices generally lack solutions by radicals (Abel–Ruffini theorem), rendering the derivation of closed-form discriminant criteria impossible. To extend the AST methodology to such complex networks, future work must integrate symbolic–numeric hybrid approaches or rely on graph-theoretic stability criteria [51] that estimate spectral radii without requiring explicit roots.

Additionally, our analysis exploits the rational structure of Holling-type functional responses. For ecological systems governed by more complex, non-smooth, or empirically fitted interaction functions, the algebraic decomposition central to AST may become intractable. In these cases, the method can be generalized by replacing exact discriminants with local Taylor approximations or by coupling the spectral radius criteria with numerical continuation software to trace bifurcation thresholds.

Despite these limitations, the framework offers a rigorous blueprint for analyzing biological feedback models. A natural next step is to complement our algebraic–spectral pipeline with finite-domain Turing analysis in a spatial PDE extension, in the spirit of the endothelial–tumor angiogenic factor stability program in [52]. Future work will also focus on developing positivity-preserving stochastic integrators for higher-dimensional systems, further strengthening the bridge between theoretical bifurcation analysis and biologically realistic modeling. Motivated by recent studies that have demonstrated that piecewise-smooth and hybrid systems can exhibit rich global behaviors, including symbolic dynamics [53], strange nonchaotic attractors [54], and Jacobi unstability [55], investigating whether such global complexity arises in the stochastic or seasonally IGP framework remains an open avenue for future research.

Use of AI tools declaration

The authors declare they have not used Artificial Intelligence (AI) tools in the creation of this article.

Conflict of interest

The authors declare there are no conflicts of interest.

References

1. A. J. Lotka, Analytical note on certain rhythmic relations in organic systems, *Proc. Natl. Acad. Sci. U.S.A.*, **6** (1920), 410–415. https://doi.org/10.1073/pnas.6.7.410
2. A. J. Lotka, Undamped oscillations derived from the law of mass action, *J. Am. Chem. Soc.*, **42** (1920), 1595–1599. https://doi.org/10.1021/ja01453a010
3. V. Volterra, Variations and fluctuations of the number of individuals in animal species living together, *J. Cons.*, **3** (1928), 3–51. https://doi.org/10.1093/icesjms/3.1.3

4. L. A. Segel, J. D. Murray: Mathematical biology (3rd Ed), volume I (an introduction) and volume II (spatial models and biomedical applications), *Math. Med. Biol.*, **20** (2003), 377–378. https://doi.org/10.1093/imammb/20.4.377
5. M. Chen, Pattern dynamics of a Lotka-Volterra model with taxis mechanism, *Appl. Math. Comput.*, **484** (2025), 129017. https://doi.org/10.1016/j.amc.2024.129017
6. C. Accarino, F. Capone, R. De Luca, G. Massa, On the dynamics of a Leslie–Gower predator–prey ternary model with intraguild, *Ricerche Mat.*, **74** (2025), 1099–1117. https://doi.org/10.1007/s11587-023-00822-9
7. R. D. Holt, G. R. Huxel, Alternative prey and the dynamics of intraguild predation: Theoretical perspectives, *Ecology*, **88** (2007), 2706–2712. https://doi.org/10.1890/06-1525.1
8. S. B. Hsu, S. Ruan, T. H. Yang, Analysis of three species Lotka–Volterra food web models with omnivory, *J. Math. Anal. Appl.*, **426** (2015), 659–687. https://doi.org/10.1016/j.jmaa.2015.01.035
9. F. Capone, M. F. Carfora, R. De Luca, I. Torcicollo, On the dynamics of an intraguild predator–prey model, *Math. Comput. Simul.*, **149** (2018), 17–31. https://doi.org/10.1016/j.matcom.2018.01.004
10. M. Arim, P. A. Marquet, Intraguild predation: A widespread interaction related to species biology, *Ecol. Lett.*, **7** (2004), 557–564. https://doi.org/10.1111/j.1461-0248.2004.00613.x
11. R. D. Holt, G. A. Polis, A theoretical framework for intraguild predation, *Am. Nat.*, **149** (1997), 745–764.
12. P. H. Leslie, J. C. Gower, The properties of a stochastic model for the predator-prey type of interaction between two species, *Biometrika*, **47** (1960), 219–234. https://doi.org/10.1093/biomet/47.3-4.219
13. A. H. Naser, D. K. Bahlool, Dynamics of an intraguild predation food web cooperation model under the influence of fear and hunting, *Computation*, **13** (2025), 128. https://doi.org/10.3390/computation13060128
14. K. Manimaran, F. Mustapha, F. M. Siam, Intraguild predation model with stage structure and cannibalism in prey population, *Matematika*, **38** (2022), 157–178. https://doi.org/10.11113/matematika.v38.n2.1410
15. S. Dash, S. Khajanchi, Dynamics of intraguild predation with intraspecies competition, *J. Appl. Math. Comput.*, **69** (2023), 4877–4906. https://doi.org/10.1007/s12190-023-01956-7
16. S. N. Raw, B. Tiwari, A mathematical model of intraguild predation with prey refuge and competitive predators, *Int. J. Appl. Comput. Math.*, **8** (2022), 157. https://doi.org/10.1007/s40819-022-01366-6
17. X. Jin, L. Liu, Y. G. Shi, Exploring coexistence and bifurcations in a tri-trophic intraguild predation model with a Holling II functional response, *Int. J. Bifurcation Chaos*, **35** (2025), 2550107. https://doi.org/10.1142/S021812742550107X
18. P. A. Abrams, S. R. Fung, Prey persistence and abundance in systems with intraguild predation and type-2 functional responses, *J. Theor. Biol.*, **264** (2010), 1033–1042. https://doi.org/10.1016/j.jtbi.2010.02.045

19. Y. Kang, L. Wedekin, Dynamics of a intraguild predation model with generalist or specialist predator, *J. Math. Biol.*, **67** (2013), 1227–1259. https://doi.org/10.1007/s00285-012-0584-z

20. D. Sen, S. Ghorai, M. Banerjee, Complex dynamics of a three species prey-predator model with intraguild predation, *Ecol. Complexity*, **34** (2018), 9–22. https://doi.org/10.1016/j.ecocom.2018.02.002

21. Z. Shang, Y. Qiao, Complex dynamics of a four-species food web model with nonlinear top predator harvesting and fear effect, *Math. Comput. Simul.*, **223** (2024), 458–484. https://doi.org/10.1016/j.matcom.2024.04.024

22. S. Chakravarty, L. N. Guin, S. Ghosh, Mathematical modelling of intraguild predation and its dynamics of resource harvesting, *Int. J. Nonlinear Anal. Appl.*, **13** (2022), 837–861. http://dx.doi.org/10.22075/ijnaa.2022.26067.3215

23. F. Farivar, G. Gambino, V. Giunta, M. C. Lombardo, M. Sammartino, Intraguild predation communities with anti-predator behavior, *SIAM J. Appl. Dyn. Syst.*, **24** (2025), 1110–1149. https://doi.org/10.1137/24M1632747

24. R. S. Cantrell, X. Cao, K. Y. Lam, T. Xiang, A PDE model of intraguild predation with cross-diffusion, *Discrete Contin. Dyn. Syst. Ser. B*, **22** (2017), 3653–3661. https://doi.org/10.3934/dcdsb.2017145

25. D. Ryan, R. S. Cantrell, Avoidance behavior in intraguild predation communities: A cross-diffusion model, *Discrete Contin. Dyn. Syst.*, **35** (2015), 1641–1663. https://doi.org/10.3934/dcds.2015.35.1641

26. P. Mishra, D. Wrzosek, Indirect taxis drives spatio-temporal patterns in an extended Schoener's intraguild predator–prey model, *Appl. Math. Lett.*, **125** (2022), 107745. https://doi.org/10.1016/j.aml.2021.107745

27. P. Mishra, D. Wrzosek, Schoener-Polis-Holt's model of the intraguild predation with predator taxis and repulsive chemotaxis, *Discrete Contin. Dyn. Syst. Ser. B*, **29** (2024), 4698–4726. https://doi.org/10.3934/dcdsb.2024062

28. Y. Ma, R. Yang, Bifurcation analysis in a modified Leslie-Gower with nonlocal competition and Beddington-DeAngelis functional response, *J. Appl. Anal. Comput.*, **15** (2025), 2152–2184. http://doi.org/10.11948/20240415

29. F. Zhu, R. Yang, Bifurcation in a modified Leslie-Gower model with nonlocal competition and fear effect, *Discrete Contin. Dyn. Syst. Ser. B*, **30** (2025), 2865–2893. https://doi.org/10.3934/dcdsb.2024195

30. R. Yang, F. Wang, D. Jin, Spatially inhomogeneous bifurcating periodic solutions induced by nonlocal competition in a predator–prey system with additional food, *Math. Methods Appl. Sci.*, **45** (2022), 9967–9978. https://doi.org/10.1002/mma.8349

31. F. Wang, R. Yang, X. Zhang, Turing patterns in a predator–prey model with double Allee effect, *Math. Comput. Simul.*, **220** (2024), 170–191. https://doi.org/10.1016/j.matcom.2024.01.015

32. H. M. Safuan, H. S. Sidhu, Z. Jovanoski, I. N. Towers, Impacts of biotic resource enrichment on a predator–prey population, *Bull. Math. Biol.*, **75** (2013), 1798–1812. https://doi.org/10.1007/s11538-013-9869-7

33. J. Yao, S. Yuan, Extinction of intra prey induced by catastrophic shift in a Lesile–Gower intraguild predation model, *Appl. Math. Lett.*, **173** (2026), 109748. https://doi.org/10.1016/j.aml.2025.109748

34. T. M. Bury, C. T. Bauch, M. Anand, Detecting and distinguishing tipping points using spectral early warning signals, *J. R. Soc. Interface*, **17** (2020), 20200482. https://doi.org/10.1098/rsif.2020.0482

35. M. M. Khan, M. J. Uddin, Chaos and bifurcations of a discretized Holling-II prey-predator model including prey refuge and Allee effect, *Sci. Rep.*, **15** (2025), 32940. https://doi.org/10.1038/s41598-025-04333-5

36. W. Yin, X. Shi, P. Meng, F. Qu, Research on recovering scattering obstacles in inhomogeneous medium based on Bayesian method, *Appl. Anal.*, **103** (2024), 3197–3212. https://doi.org/10.1080/00036811.2024.2346275

37. J. Zhuang, P. Meng, W. Yin, A stable neural network for inverse scattering problems with contaminated data, *Knowledge-Based Syst.*, **310** (2025), 113001. https://doi.org/10.1016/j.knosys.2025.113001

38. P. Meng, Z. Xu, X. Wang, W. Yin, H. Liu, A novel method for solving the inverse spectral problem with incomplete data, *J. Comput. Appl. Math.*, **463** (2025), 116525. https://doi.org/10.1016/j.cam.2025.116525

39. Y. Deng, H. Liu, L. Zhu, Optimal estimate of electromagnetic field concentration between two nearly-touching inclusions in the quasi-static regime, *SIAM J. Math. Anal.*, **57** (2025), 2596–2621. https://doi.org/10.1137/24M1639774

40. H. Diao, H. Liu, Q. Meng, L. Wang, Effective medium theory for embedded obstacles in electromagnetic scattering with applications, *J. Differ. Equations*, **437** (2025), 113283. https://doi.org/10.1016/j.jde.2025.113283

41. V. Makler-Pick, M. R. Hipsey, T. Zohary, Y. Carmel, G. Gal, Intraguild predation dynamics in a lake ecosystem based on a coupled hydrodynamic-ecological model: The example of Lake Kinneret (Israel), *Biology*, **6** (2017), 22. https://doi.org/10.3390/biology6020022

42. M. A. Aziz-Alaoui, M. D. Okiye, Boundedness and global stability for a predator-prey model with modified Leslie-Gower and Holling-type II schemes, *Appl. Math. Lett.*, **16** (2003), 1069–1075. https://doi.org/10.1016/S0893-9659(03)90096-6

43. L. Perko, *Differential Equations and Dynamical Systems*, 3nd edition, Springer-Verlag, New York, 2001.

44. P. S. Mandal, L. J. S. Allen, M. Banerjee, Stochastic modeling of phytoplankton allelopathy, *Appl. Math. Modell.*, **38** (2014), 1583–1596. https://doi.org/10.1016/j.apm.2013.08.031

45. R. V. dos Santos, Discreteness inducing coexistence, *Phys. A*, **392** (2013), 5888–5897. https://doi.org/10.1016/j.physa.2013.07.058

46. G. W. A. Constable, T. Rogers, A. J. McKane, C. E. Tarnita, Demographic noise can reverse the direction of deterministic selection, *Proc. Natl. Acad. Sci. U.S.A.*, **113** (2016), E4745–E4754. https://doi.org/10.1073/pnas.1603693113

47. H. Weissmann, N. M. Shnerb, D. A. Kessler, Simulation of spatial systems with demographic noise, *Phys. Rev. E*, **98** (2018), 022131. https://doi.org/10.1103/PhysRevE.98.022131

48. M. Abundo, A stochastic model for predator-prey systems: Basic properties, stability and computer simulation, *J. Math. Biol.*, **29** (1991), 495–511. https://doi.org/10.1007/BF00164048

49. L. S. Wang, J. Yu, Analysis framework for stochastic predator–prey model with demographic noise, *Results Appl. Math.*, **27** (2025), 100621. https://doi.org/10.1016/j.rinam.2025.100621

50. L. S. Wang, J. Yu, S. Li, Z. Liu, Analysis and mean-field limit of a hybrid PDE-ABM modeling angiogenesis-regulated resistance evolution, *Mathematics*, **13** (2025), 2898. https://doi.org/10.3390/math13172898

51. F. Solimano, E. Beretta, Graph theoretical criteria for stability and boundedness of predator-prey systems, *Bull. Math. Biol.*, **44** (1982), 579–585. https://doi.org/10.1007/BF02459411

52. Z. Liu, L. S. Wang, J. Yu, J. Zhang, E. Martel, S. Li, Bidirectional endothelial feedback drives Turing-vascular patterning and drug-resistance niches: A hybrid PDE-agent-based study, *Bioengineering*, **12** (2025), 1097. https://doi.org/10.3390/bioengineering12101097

53. J. Duan, Z. Wei, D. Li, H. Su, C. Grebogi, Symbolic dynamics for a kinds of piecewise smooth maps, *Discrete Contin. Dyn. Syst. Ser. S*, **17** (2024), 2778–2787. https://doi.org/10.3934/dcdss.2024042

54. J. Duan, Z. Wei, G. Li, D. Li, C. Grebogi, Strange nonchaotic attractors in a class of quasiperiodically forced piecewise smooth systems, *Nonlinear Dyn.*, **112** (2024), 12565–12577. https://doi.org/10.1007/s11071-024-09678-6

55. Z. Wei, F. Wang, H. Li, W. Zhang, Jacobi stability analysis and impulsive control of a 5D self-exciting homopolar disc dynamo, *Discrete Contin. Dyn. Syst. Ser. B*, **27** (2022), 5029–5045. https://doi.org/10.3934/dcdsb.2021263

AIMS Press